Multiscale CFD Modeling of Area-Selective Atomic Layer Deposition: Application to Reactor Design and Operating Condition Calculation

Sungil Yun [1], Henrik Wang [1], Matthew Tom [1], Feiyang Ou [1], Gerassimos Orkoulas [2] and Panagiotis D. Christofides [1,3,*]

1   Department of Chemical and Biomolecular Engineering, University of California, Los Angeles, CA 90095, USA
2   Department of Chemical Engineering, Widener University, Chester, PA 19013, USA
3   Department of Electrical and Computer Engineering, University of California, Los Angeles, CA 90095, USA
*   Correspondence: pdc@seas.ucla.edu; Tel.: +1-(310)-794-1015

Abstract: Area-selective atomic layer deposition (ASALD) as a bottom-up nanopatterning technique has gained recognition for its ability to address misalignment issues in semiconductor manufacturing. This in silico study investigates process operation conditions for ASALD of SiO_2/Al_2O_3 and reactor optimization by using multiscale computational fluid dynamics (CFD) modeling. Several reactor designs were modeled in Ansys Workbench and their results compared to ensure effective reagent separation and homogeneous exposure to reagents across the wafer. Annular reaction zones and asymmetrical inlets enhanced uniform exposure to reagents and minimized reagent intermixing, which allowed the reactor to tolerate higher rotational speeds. Additionally, low rotation speeds and high species mole fractions were required for complete deposition of a cycle of the ASALD process. This research provides insight into the ASALD process operation and contributes to further industrial versatility.

Keywords: area-selective atomic layer deposition; spatial reactors; kinetic Monte Carlo; computational fluid dynamics; semiconductor manufacturing

1. Introduction

The last decade has seen a rise in the performance and downscaling of technology due to the successful commercialization of 5-nm Fin-Field Effect Transistors (FinFETs), which is attributed to the newly developed, state-of-the-art extreme ultraviolet (EUV) lithography technology [1]. The semiconductor industry is now presumably on the verge of entering the 3-nm process era [2,3], thereby meeting the projections of Moore's Law. To further miniaturize and improve nanochip performance, the stacking of transistors to assemble elaborate three-dimensional (3D) structures is being implemented in nanodevices [4], and the number of levels of stack is increasing significantly [5]. However, chipmakers are facing a challenge where vertically stacked features are often displaced from their original positions as the feature sizes of electronic devices continue to shrink [6]. To maximize chip performance, device features on 3D structures must be positioned with extreme precision in the nanoscale, which poses an obstacle for transistor assemblage. If devices are not aligned properly and features are not placed in precise locations, it may lead to a misalignment or an edge placement error (EPE) [7]. The misalignment of features in 3D semiconductor chip stacks needs to be resolved, as this issue also causes structures to be deformed [8,9]. Structure deformation disrupts the flow of electric currents, further increasing the likelihood of chip failure [10]. It has been reported that these misalignment issues are associated with the conventional top-down fabrication methodology of using a series of deposition, lithography, and etching processes [11]. The top-down process is

defined as the one that carves out large structures in the substrate to build a feature in a subtractive fashion. This top-down paradigm has definitely contributed to the existence of the modern 3D FinFET device. However, it has also limited the number of layers that can be vertically stacked due to the stacking displacement.

As a compelling alternative that avoids the issue of misalignment, the bottom-up fabrication technique has gained momentum in recent years [12]. In this bottom-up synthesis method, molecules are scaled up to build nanoscale features from reactive precursors in a self-aligned manner that requires energetically favorable operating conditions [13] and low surface defect densities [14] to yield anisotropic layering. However, the generation of self-aligned structures allows for greater control over the morphologies of the patterned surface and reduces EPEs while enabling smaller feature sizes for wafers [15]. Currently, self-assembled nanostructures are constructed using lithographic techniques [16] to generate templates preceding thin-layer deposition to promote nanopatterning [17] in this bottom-up approach. Recently, researchers have focused on self-assembling nanostructures such as [18] who studied the chemoselective nature of a chemical inhibitor on chemically similar metal-oxides and [19] who proposed a new precursor passivation technique that was beneficial for promoting higher controllable surface morphologies. In particular, a nanowire, as a high aspect-ratio component of a transistor [20,21] that is capable of being synthesized in one-dimensional (1D) structures [11], has been recognized for its potential to fabricate gate-all-around (GAA) transistors [22]. Apart from self-assembly, the bottom-up process is leveraged by a nonlithographic technique proposed in [23] and demonstrated in [24]. This emerging technology is conducive toward reducing manufacturing costs [25], eliminating lithography-related processes, and therefore, minimizing toxic reagents [26] that are used in nanoimprint lithographic methods [27]. Area-selective atomic layer deposition (ASALD) is a promising candidate as a bottom-up fabrication process that addresses the challenges of limiting multilayer stacking [26]. ASALD is a technique that locally deposits materials on the growth area (GA), enabling self-aligned fabrication by reducing EPEs [28,29]. To achieve area-selective atomic layer deposition, it is essential to protect the top surface of the non-growth area (NGA) with surface modifying reagents or inhibitors. In this manner, inhibitors passivate the surface of the NGA by creating protective layers to hinder ALD growth on the NGA. Thus, ALD growth is permitted only on the GA in chemoselective and regioselective behaviors. Inhibitor selection obviously plays an essential role to accomplish successful area-selective ALD, and several, long, aqueous polymeric chain inhibitors have been experimented, such as octadecyltrichlorosilane (ODTS) [28,30] and poly(methyl methacrylate) (PMMA) [31]. Additionally, gaseous small molecule inhibitors (SMIs) have been explored as a promising method [9,32] since the degradation of protective coatings is insignificant, and SMI-based ASALD is readily integrated with various vapor-phase ALD reactions [33].

However, it has been demanding to further commercialize and optimize ASALD technology due to the difficulty of gaining an in-depth understanding of the process [29]. Even though experimental approaches are of value, not only are those experiments costly and time-consuming, but in situ monitoring is also restricted, resulting in a lack of spatiotemporal data. in silico studies using multiscale modeling addresses these issues by simultaneously analyzing the features of surface kinetics and fluid flow throughout reactors in a cost-effective manner. Therefore, in conjunction with experimental methods, the development of multiphysics models is needed to offer high-fidelity fluid dynamics data and robust guidelines for process operation and control. The study of multiscale modeling is separated into three parts: (1) atomistic-mesoscopic modeling that characterizes the surface reaction mechanism using kinetic Monte Carlo (kMC) simulations and ab initio Density Functional Theory (DFT) calculations, (2) computational fluid dynamics (CFD) modeling that produces diverse data sets for multiphysics fluid flow, and (3) the design of optimal control systems that ensures high-quality output and stable operation. The first step of developing an atomistic-mesoscopic model to delineate thin-film surface kinetics with steric repulsion effects for area-selective ALD of SiO_2/Al_2O_3 in which the SMI, acetylacetone

(Hacac), precursor, bis(diethylamino)silane (BDEAS), and oxidant, ozone, are utilized for Steps A through C, respectively, was successfully carried out [34]. In this paper, as the second step, a multiscale model which combines the atomistic-mesoscopic model and a macroscopic model is developed to offer insight for further industrialization.

Recently, there has been growing interest in spatial atomic layer deposition, which is a potential substitute for conventional ALD processes in that it is capable of high-volume manufacturing [35]. This high throughput capability is made possible by the injection of reagents into separate reaction zones within the spatial reactor that are isolated with an inert gas curtain and vacuum zones. Figure 1 depicts the schematic diagram of a sheet-to-sheet spatial ALD reactor configuration where the substrate is transferred between reaction zones that are isolated by inert gases (gas curtain) by a conveyor belt. Due to the spatially separated reaction zones, no lengthy purging steps are required to maintain the self-limiting nature of the reactions. In other words, spatial ALD is able to save a significant amount of purging time, resulting in a high throughput ALD process. There have been various proposals of different spatial ALD reactor configurations. The original concept of a spatial reactor as a roll-to-roll reactor was first proposed in 1977 [36], of which applications were limited to flexible substrates. Afterward, a few sheet-to-sheet designs for solar photovoltaic technology and other applications have been developed and commercialized [37,38]. Recent in silico research into multiphysics simulations have focused on sheet-to-sheet designs to provide valuable insight into a route for further industrialization. For instance, several works have explored the effects of the gap distance, which is the separation distance between the dividers and surface of the substrate in Figure 1, on the flow dynamics [39] as well as reactor operating conditions including pumping pressure and substrate velocity [40,41]. Furthermore, ref [42] examined how precursor flow rates and other process operating parameters impact on transport phenomena and surface reactions. Additionally, prior works [43,44] investigated the effect of the substrate velocity on film uniformity and surface kinetics using a three-dimensional multiscale computational fluid dynamics model. Despite the potential of high-volume production, the sheet-to-sheet reactors weaken in terms of versatile applications since it is impossible to avoid necessitating larger equipment with longer substrates compared to standardized wafers. As another approach, rotary designs have been experimented on a laboratory scale, and they have demonstrated the operational capability to provide uniform film growths [45,46]. Furthermore, the dimensions of rotary designs are comparable to that of stationary ALD reactors. Nevertheless, a few studies have carried out experiments to evaluate the rotary design [46,47]. Moreover, aforementioned in silico studies have solitarily focused on the sheet-to-sheet type reactors, which are significantly different from rotary type reactors in many aspects including transport phenomena, reactor configuration optimization, and control strategies. At this stage, research studies aided by computational fluid dynamics simulations are needed to thoroughly investigate the surface kinetics in conjunction with the fluid dynamics of rotary designs.

Therefore, in this study, a computational simulation method, the so-called multiscale model, is presented to qualitatively and quantitatively analyze the features of a rotary spatial ALD reactor design and the ABC-type ASALD process in an operable ALD window. The structure of this paper is as follows: Section 2.1 describes the methodology of integrating an atomistic-mesoscopic model and a macroscopic model, Section 2.2 illustrates atomistic-mesoscopic modeling with kinetic descriptions, Section 2.3 explains the methodology of macroscopic modeling, Section 3 discusses the results of the multiscale modeling work, and finally, Section 4 encapsulates the conclusion of this work.
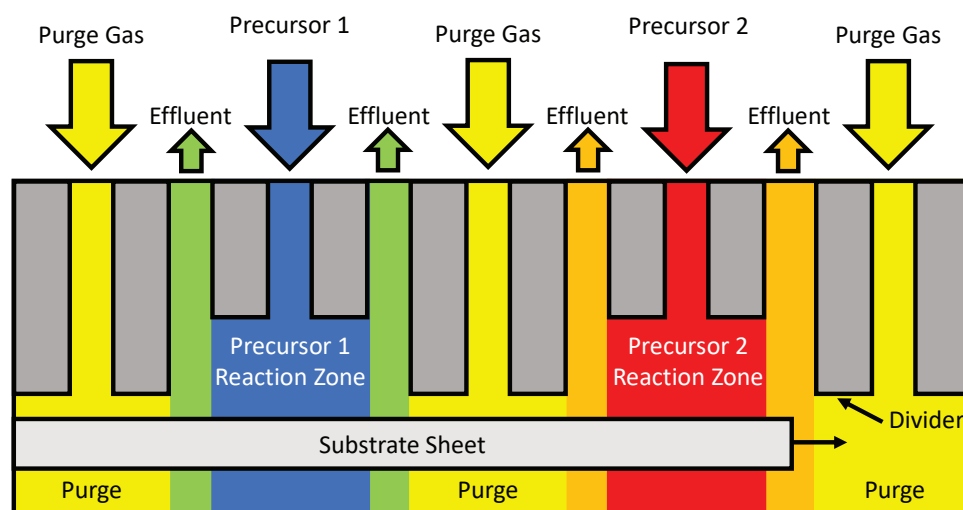
Figure 1. Sheet to sheet type reactor design for a two-step, spatial atomic layer deposition process. Reagents are continuously introduced in separate reaction zones, and a plate-shaped substrate is transported via a conveyor belt through each zone.

2. Multiscale Modeling

2.1. Multiscale Modeling Framework

It is desired to establish a quantitative relationship between the mesoscale surface kinetics on the substrate surface and the macroscopic fluid dynamics of the reactor to provide an effective and reproducible method for accurately simulating the overall process through a multiscale modeling framework [48]. Additionally, multiscale models are capable of modeling through various time and length scales, as illustrated in Figure 2. In this work, a multiscale model is developed by integrating an atomistic-mesoscopic and a macroscopic simulation that are conjoined by a data-sharing programming methodology. This new model operates without requiring robust computational resources through appropriate process assumptions and simplifications, and provides an accurate representation of realistic phenomena encountered in industrial settings that have been incorporated into this work.

The atomistic-mesoscopic model of the ABC-type ASALD of SiO_2/Al_2O_3 surfaces with a SMI was first developed by [34], and it will be integrated into the multiscale model of this work. For the purposes of this work, the atomistic-mesoscopic model will be referred to as the mesoscopic model for simplicity. The mesoscopic model conjoins first principles ab initio quantum mechanics (e.g., Density Functional Theory and Nudged Elastic Band) and statistical mechanics (e.g., Transition State Theory and Collision Theory) to evaluate reaction rate constants that will be integrated into a kinetic Monte Carlo algorithm to monitor the surface kinetics. While the mesoscopic simulation records the evolution of surface kinetics, a macroscopic model is needed to examine the continuum mechanics in the ambient fluid conditions. A three-dimensional computational fluid dynamics (CFD) simulation is employed to observe the spatiotemporal behavior of the species and fluid dynamics in a reaction chamber through a rigorous process of reactor optimization, mesh discretization, and tailoring the macroscopic model to the ASALD reactor (e.g., boundary conditions, user-defined functions, numerical solver methods, and operating conditions). From the development of the mesoscopic and macroscopic domains, the simulations are conjoined by linking the surface partial pressure data evaluated from the macroscopic CFD model to the kMC simulation, which successively evaluates the source accumulation rates of species for a time progression to be defined to the macroscopic CFD model. Thus, a multiscale model is intimately constructed that enables the simultaneous modeling of surface kinetics and continuum mechanics in a spatiotemporal manner, which is depicted by the process diagram in Figure 3.
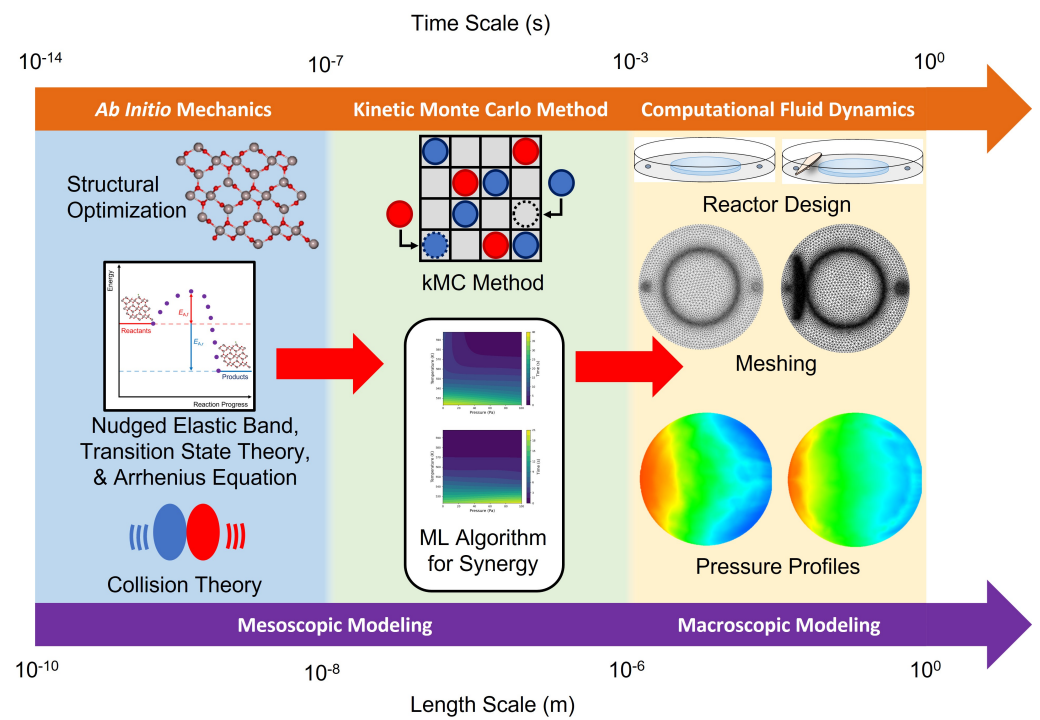
Figure 2. Diagram depicting the various length and time scales applicable for the multiscale modeling simulation, which is composed of mesoscopic and macroscopic modeling. Mesoscopic modeling is composed of ab initio quantum and statistical mechanics and the kinetic Monte Carlo method, and the macroscopic model consists of reactor modeling and computational fluid dynamics simulations. Prior work [49] has utilized machine learning or regression methods to determine optimal operating conditions to achieve high synergy.
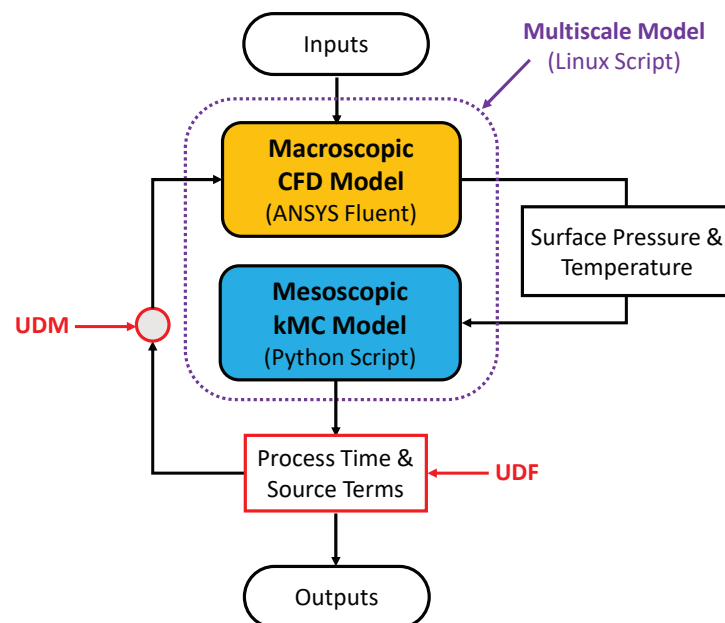

Figure 3. Coding architecture of the multiscale simulation using various programming languages to conjoin the mesoscopic and macroscopic simulations. In a Linux Shell script as an interface between the macroscopic and mesoscopic models, two models are simulated while exchanging pressure, temperature, and source generation (or consumption) with each other.

2.2. Mesoscopic Model

2.2.1. Surface kinetics

The abundance of undetermined reaction pathways present a challenge for defining the overall reaction mechanism for each step in the ASALD process. One methodology is to simplify the reaction mechanism to purely consist of rate determining reactions that are also elementary. Thus, the surface chemistries involved in ASALD of SiO_2/Al_2O_3 are selected from experimental works [9,50]. Below, the proposed reaction pathways for each step in the ABC-ASALD process are summarized. There are three reactions that the mesoscopic model must simulate that together make up one ASALD cycle. The first reaction, Step A, is where acetylacetone (Hacac) adsorbs to Al_2O_3 to act as an inhibitor on the non growth area. This reaction has the following steps:
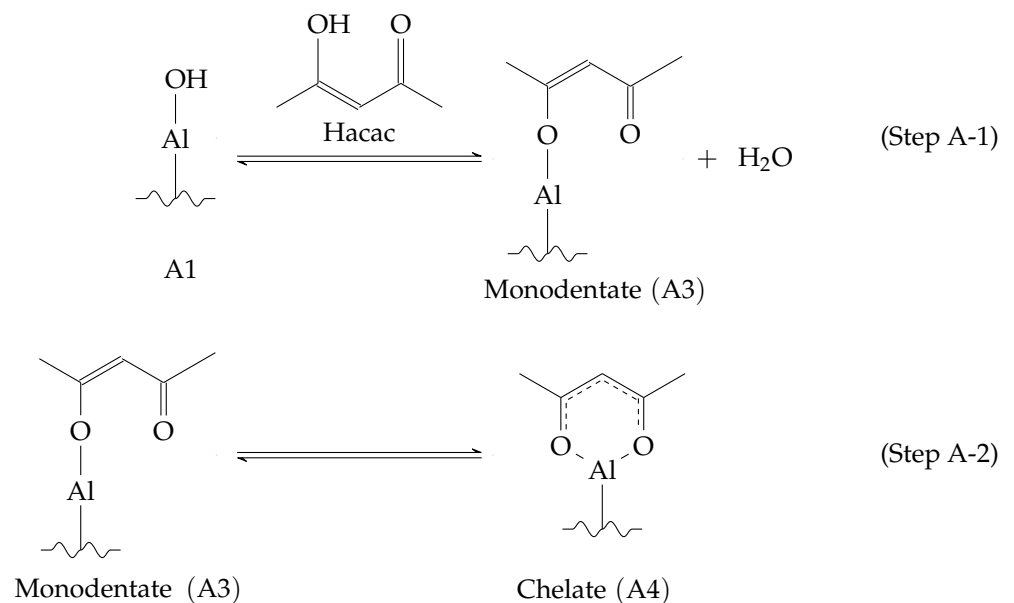
(Step A-1)

(Step A-2)

In Step A-1, an acidic, keto-enol tautomerized Hacac molecule reacts with the basic hydroxyl group on the Al_2O_3 surface, which produces water vapor as a byproduct. Then, in the following step, the monodentate structure of the adsorbed Hacac undergoes a rearrangement mechanism to produce a more stable, chelate form.

The second reaction, Step B, is composed of an adsorption step of bis(diethylamino)silane (BDEAS) onto SiO_2 to propagate the growth of a monolayer of SiO_2, which is referred to as the growth area. Analogously to Step A, this reaction also consists of two steps:

(Step B-1)

(Step B-2)

V3   V4   DEA
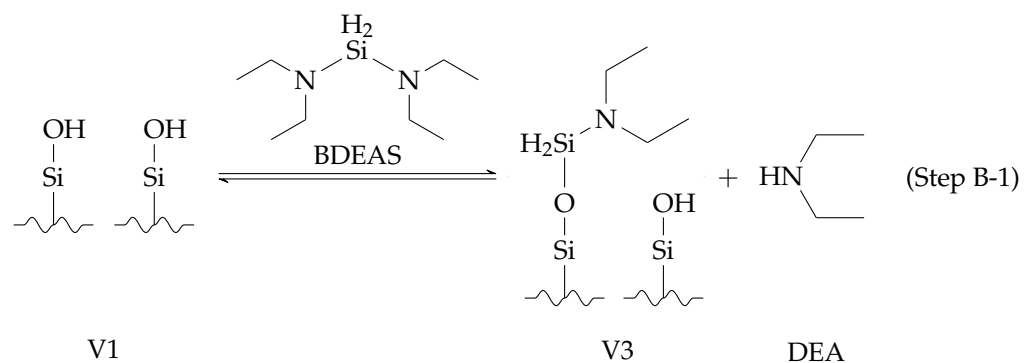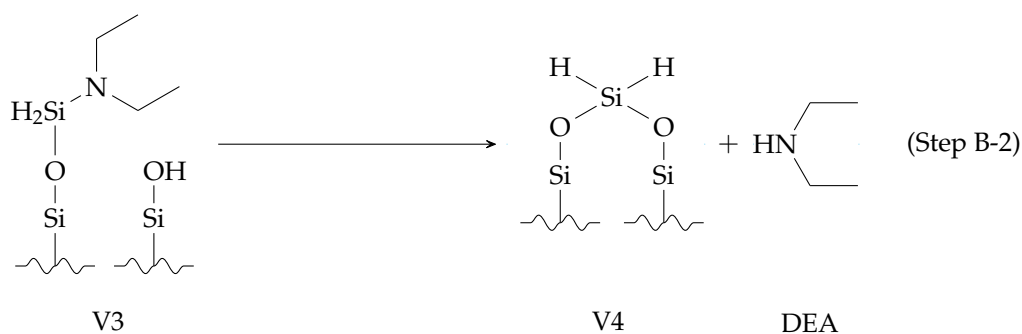
In Step B-1, the bulky BDEAS molecule adsorbs to one hydroxyl site on SiO_2, which produces one molecule of diethylamine (DEA) as a byproduct. In Step B-2, the BDEAS molecule binds to an adjacent hydroxyl site on SiO_2, which produces a second DEA molecule as a byproduct. After Step B is completed, a monolayer of silicon atoms will have been deposited on the original SiO_2 surface.

Finally, the third reaction, Step C, is where the monolayer of Si is oxidized with O_3 to finish growing the layer of SiO_2. Its reactions have the following form:

(Step C-1)

V4   V6

(Step C-2)

V6   V8
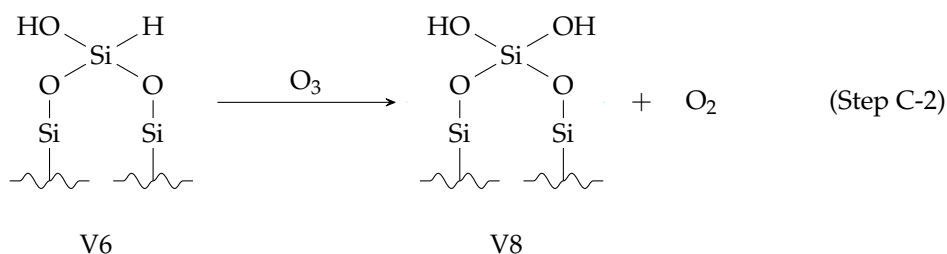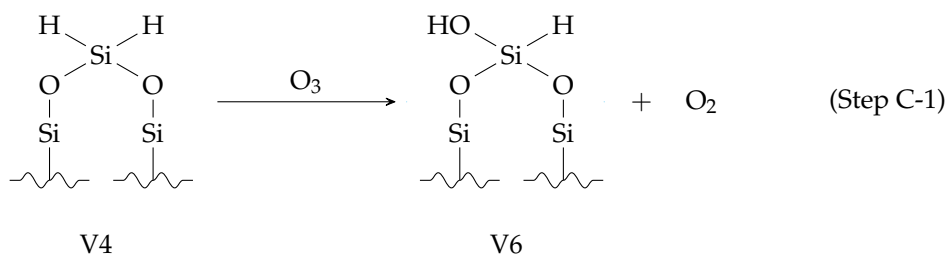
Here, two ozone atoms are consumed per Si atom, leading to a homogeneous array of geminal hydroxylated ligands of SiO_2 with two O_2 atoms as the byproduct. For the kMC algorithm, the kinetic rate constants of all reactions (above) including physisorption and desorption of the reagents must be evaluated as a function of temperature and partial pressures. Detailed descriptions of the reaction pathways and kinetic parameters can be found in [34].

2.2.2. Quantification of Surface Reactions

Various ab initio quantum and statistical mechanics as well as first-principles physical chemistry approaches were integrated into this work to evaluate the reaction rate constants for each reaction. This section discusses the theoretical approaches for computing the reaction rate constants for each reaction, which are categorized into two classes: nonadsorption or adsorption.

For nonadsorption reactions, their reaction rate constants are calculated using the Arrhenius equation, which requires the activation energy and pre-exponential terms to be computed. The first step towards the computing of these reaction rate constants is to generate an optimized crystalline and molecular structure of the reactants and products of the nonadsorption reactions. One underlying assumption of these optimized molecular

and crystalline structures is that the surface of the wafer, which is amorphous in nature, is simplified to a homogeneous crystalline structure [51,52] and is modeled without the presence of crystallographic defects. This procedure has been conducted in prior microscopic and mesoscopic modeling of atomic layer etching and area-selective atomic layer deposition processes to alleviate the computational burden of the simulation and to reduce the complexity of the coding architecture for the kMC simulation while maintaining some structural fidelity [34,49]. The computations for structural optimization are achieved by employing the open-source molecular dynamics program, Quantum ESPRESSO [53], to perform a structural optimization of the lattice structure of the solid materials and the molecular structure of the gaseous species. This procedure is conducted by finding the minimum, total electronic energy of the species, E_{total}, through tuning the independent parameters $\mathbf{k}$, E_ψ, and E_ρ, which are the *k*-points (specified as *automatic*), the kinetic energy cut-off for wave functions (*ecutwfc*), and the kinetic energy cut-off for charge density and potential (*ecutrho*), respectively, in an iterative procedure until a convergence threshold specified to the program is satisfied. The parameters $\mathbf{k}$, E_ψ, and E_ρ, are adjusted until the infimum of the total electronic energy is obtained, which is described below:

$$\inf_{\mathbf{k}\in\mathbb{R}^6, E_\psi\in\mathbb{R}, E_\rho\in\mathbb{R}} E_{\text{total}}\left(\mathbf{k}, E_\psi, E_\rho\right) \tag{1}$$

Following the molecular optimization procedure, the nudged elastic band (NEB) method is employed to evaluate the activation energies for the nonadsorption reactions. The NEB approach is a transition-path sampling procedure that identifies saddle points to determine the minimum energy path between the reactant(s) and product(s) by generating a user-defined number of images of the conversion and atomic movement for each molecular structure [54]. Although a higher number of images (intermediate transition states with minimum energy path) is essential for computing molecular properties of high fidelity, such a simulation will require greater computational resources to complete in ample time as well; therefore, a total of nine images were used in a prior work [34] with results that were verified to experimentally recorded data results observed by [9,33,50]. Once all the intermediate images are produced along with the saddle point, the maximum energy peak is determined, which is utilized to compute the activation energy for the forward and reverse reactions. With the activation energy, the reaction rate constant for each nonadsorption reaction is calculated with the Arrhenius equation, which is shown below:

$$k_{nonad} = \nu \exp\left(-\frac{E_{act}}{RT}\right) \tag{2}$$

where k_{nonad} is the reaction rate constant for a nonadsorption reaction, ν is the temperature dependent pre-exponential factor, E_{act} is the activation energy of the reaction, R is the universal gas constant, and T is the absolute temperature of the reaction. The calculation of the pre-exponential factor is simplified by assuming that the ratio between the transition state and reactant partition functions is unity [55]. This yields the following equation for the pre-exponential factor ν, which is dependent on the temperature, T, of the reaction:

$$\nu = \frac{k_B T}{h} \tag{3}$$

where k_B is the Boltzmann constant and h is the Planck constant.

For adsorption reactions, it is simpler to calculate their reaction rate constants, which are modeled as bimolecular reactions that follow Maxwell-Boltzmann statistics and Collision Theory. The reaction rate constants for adsorbate species, s, are then characterized by the following equation:

$$k_{ads,s} = \frac{P_s A_{site} \sigma_s}{Z_s \sqrt{2\pi m_s k_B T}} \tag{4}$$

where $k_{ads,s}$ is the reaction rate constant for an adsorption reaction, P_s is the partial pressure of the gaseous reagent, s, A_{site} is the surface area of a single active site, σ_s is an experimentally determined sticking coefficient unique to the reagent s, Z_s is the coordination number of the gas s, m_s is the atomic mass of the gaseous reagent s, k_B is the Boltzmann constant, and T is the absolute temperature of the ambient environment. The sticking coefficient was found for Hacac to be 1.0×10^{-4} [56], that of BDEAS to be 2.0×10^{-5} [57], and that of O_3 to be 4.5×10^{-5} [58]. In [34], these sticking coefficients were validated through comparison to experimental results from [33].

2.2.3. kMC Algorithm

After characterizing the various reaction parameters through ab initio quantum and statistical mechanics simulations as described above, the computationally efficient kinetic Monte Carlo (kMC) algorithm is integrated into the mesoscopic model simulation. The kMC algorithm is an approach that uses randomly generated numbers to reflect the stochastic and chaotic behavior of reactions occurring on the atomic scale [59]. This practice is used to model the adsorption and interchanging of various species on the surface of the substrate in this study. The procedure involves the weighting of potential reactions occurring on active sites using a random number, which are discretized into a 300×300 array in the Python programming language, resulting in 90,000 reaction sites in total. Following the random selection of the reaction using the first random number, the duration of the reaction progression is then evaluated through a secondary random number that is independent of the first random number. A summary of the procedures from [55] are described below and illustrated in Figure 4:
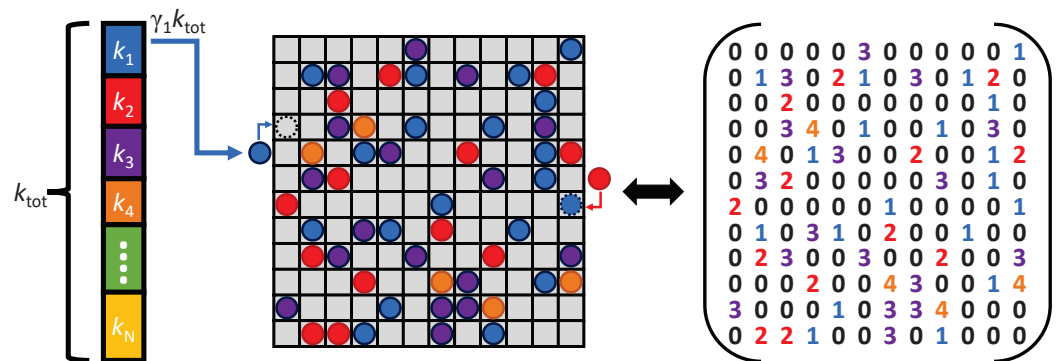

Figure 4. Kinetic Monte Carlo simulation on lattice diagram. For each reaction site, an identifiable number is allocated corresponding to a reaction if the selection condition of a certain reaction path is satisfied in Equation (6).

$$k_{tot} = \sum_{i-1}^{N} k_i \tag{5}$$

where k_{tot} is the sum of all possible reaction rate constants, k_i is the reaction rate constant for the ith potential reaction in the reaction mechanism, and N denotes the total number of possible reaction pathways for the lattice site.

The kMC method establishes a stochastic procedure by randomly assigning a number, $\gamma_1 \in (0, 1]$ to select one of the reaction rate constants that were weighted during the prior summation procedure [59]. Larger reaction rates will have a higher probability for selection due to the weighting procedure, which is also consistent with the nature of kinetics in favoring reaction processes with higher reaction rate constants or lower activation energies.

$$\sum_{i=1}^{j-1} k_i \leq \gamma_1 k_{tot} \leq \sum_{i=1}^{j} k_i \tag{6}$$

Above, j represents the reaction index chosen from the N possible reactions. If the above equation is satisfied, the reaction j is selected for the reaction at the site. If the selection procedure for all reaction sites is complete, lastly, the time progression in which the site of reaction is undisturbed is evaluated using a secondary random number, $\gamma_2 \in (0, 1]$.

$$\Delta t = \frac{-\ln(\gamma_2)}{k_{tot}} \tag{7}$$

Although the kMC algorithm provides an efficient procedure for predicting the occurrence of a reaction, it alone is not enough to provide an accurate description of the overall kinetics. While activation energy barriers ultimately dictate the directionality of reactions, other factors such as steric hindrance affect the probability of a successful adsorption reaction. The steric hindrance originates from the bulkiness of the Hacac and BDEAS molecules in Steps A and B as the molecules must adsorb to multiple active sites to fully adhere to the SiO_2/Al_2O_3 surface. When these two molecules adsorb to an active site on their respective substrates, the adsorbates are bulky that they inhibit adjacent active sites from properly binding to other molecules, thereby generating atomic vacancies. Thus, the kMC algorithm must be modified to account for these physical limitations by exercising a novel methodology that simulates hindered sites. In a prior study, ref [34] performed this modification to the kMC algorithm by modeling the adsorption of individual Hacac and BDEAS molecules by considering their orientations on the site of adsorption, which is integrated into the multiscale modeling framework in this work.

The kinetic model described above was validated by comparing the in silico simulation results of Hacac adsorption on Al_2O_3 to reported experimental results of the same reaction. The kinetic model simulated a chelate surface density of 1.45 ± 0.02 molecules/nm^2 [34] while experimental results determined a chelate surface density of 1.7 ± 0.1 molecules/nm^2 [33]. This deviation is attributed to the longer atomic distances calculated with Quantum ESPRESSO compared to the shorter atomic distances observed by [33]. Additionally, the ratio of Hacac chelate to monodentates is also comparable with experimental findings. The kinetic model simulation computed a monodentate fraction of $19.37 \pm 1.40\%$ [34] while the experimental value of monodentate fraction was found to be $20 \pm 5\%$ [33] through infrared (IR) spectroscopy. Furthermore, the computed process time to achieve full coverage for the mesoscopic simulation was determined to be similar to results conducted in experimental laboratory settings [34]; thus, the kMC algorithm is incorporated into the multiscale model with confidence.

2.3. Macroscopic Model

2.3.1. Macroscopic Modeling Logistics

The macroscopic model consists of preprocessing and postprocessing procedures that are intended to simulate fluid dynamics for the ASALD process. First, reactor configurations are assembled through computer aided design (CAD) software. The configurations are optimized computationally through a mesh of reasonable quality which ensures lower simulation times and higher substrate quality. Once the reactor model is fully developed, the simulation is tailored to the ASALD process environment by customizing various solver, physics, and personalized settings such as boundary conditions, numerical solver methods, convergence criteria, user-defined functions, materials, fluid dynamics conditions, and remeshing methods. This section will discuss the various settings that are integrated into the macroscopic computational fluid dynamics (CFD) simulation.

Ansys Workbench (2022R2), a simulation integration platform, is used to access various applications for constructing reactors through computer aided design (CAD) software, performing discretized meshing, and conducting computational fluid dynamics (CFD) simulation. In Ansys Workbench, Ansys DesignModeler is used to build reactor geometries while the spatiotemporal fluid dynamics of the gas-phase domain inside the designed reactor configurations are simulated using Ansys Fluent.

2.3.2. Reactor Geometry and Meshing

Different rotary type reactor configurations are devised, which originate from industrial patents [60]. Figure 5 illustrates the schematic representation of the spatial reactor designs to investigate flow profiles. **R1** has a ring-shaped outlet for each reaction zone and 6 10-mm round inlets (3 for the reagents and 3 for nitrogen), as depicted in Figure 5a. Meanwhile, Figure 5b shows **R2**, and it is designed with three ring, sector-shaped outlets and 6 round inlets. **R3** features asymmetrical round inlets compared to **R2** as shown in Figure 5c. Figure 5d reveals that **R4** is equipped with a ring, sector-shaped N_2 inlet for each reaction zone, enclosing a ring, sector-shaped outlet and an asymmetrical annular, sector-shaped reagent inlet. Each reactor is designed with a diameter of 760 mm, in which three wafers with a diameter of 200 mm are mounted on the rotating plate at the bottom of the reactor. The rotating plate spins, causing the wafers to encounter the reaction zones A, B, and C sequentially. The gas distribution assembly consists of differently shaped inlets, outlets, and vacuum ports and is located on top of the reactor. With **R1** through **R4**, the effects of the differences in geometry are qualitatively and quantitatively analyzed to propose an optimal reactor geometry. Finally, with the selected reactor design, process operation with different operating conditions is explored through multiscale simulations.
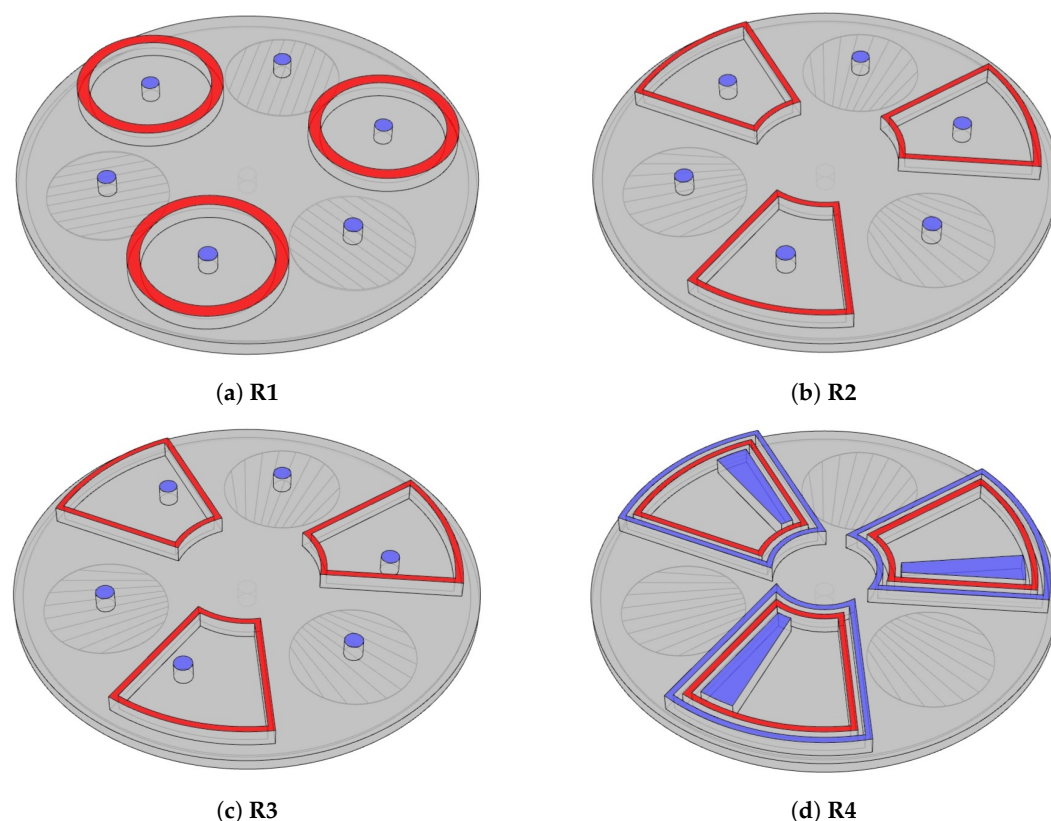

(a) R1	(b) R2

(c) R3	(d) R4

Figure 5. Four types of spatial, rotary ASALD reactor models with various inlet and outlet geometries (ring or annular sector) and positioning (symmetric or asymmetric) of reagent inlets. Red and blue areas indicate the outlets and inlets, respectively. 3 wafers are placed at the bottom inside the reactors.

In this study, the operating pressure of the reactor and the vacuum pressure of the outlets are set to 1330 Pa and −150 Pa, respectively, and the temperature is set to 523 K. These conditions are considered typical for silicon oxide deposition [9,50]. It is assumed that a PID (proportional-integral-derivative) controller regulates the operating temperature on each wafer surface so that the temperature of the wafers is maintained at a constant temperature of 523 K. The three reagents (Hacac, BDEAS, and ozone) are injected through separate inlet ports as a gas mixture with inert gas, N_2. It was reported that there is no significant temperature dependence in the ASALD process [34,50]; therefore, multiscale

simulations are performed with a fixed temperature of 523 K while rotation speed is varied in the range of 0.2 to 0.8 rad/s and the mole fractions of the reagents are varied in the range of 0.05 to 0.7 each in Section 3.2.

The meshing package on Ansys Workbench is used to generate high-quality meshes. Mesh discretization is conducted to obtain numerical solutions by adopting the finite volume method, and has a significant impact on the accuracy of the solution. Tetrahedral elements are chosen as they are recommended for 3D geometries by providing high mesh convergence. For mesh sizing, proximity, and curvature, refinements are conducted to capture more accurate flow profiles in thin reactor configurations. In addition, the face mesh of the outlets (i.e., vacuum ports) is enhanced through face meshing controls to determine the suitable divisions of the face mesh. To capture the motion of the rotating boundaries, the dynamic mesh model is necessary for modeling flow dynamics spatiotemporally. This feature facilitates the process for updating the volume mesh while preserving the quality of the mesh. The mesh quality of the reactor configurations that are developed in this paper is summarized in Table 1. The constructed meshes are qualified for CFD simulations in accordance with the standardized ranges provided by [61].

Table 1. Average values of mesh quality factors for various rotary reactor configurations.

No.	* Skewness	** Orthogonal Quality	*** Element Quality	**** Aspect Ratio
R1	0.2536	0.7446	0.8194	1.9136
R2	0.2471	0.7512	0.8244	1.8949
R3	0.2469	0.7514	0.8246	1.8933
† **R4**	0.2483	0.7499	0.8239	1.8971

* Excellent (0–0.25), Very good (0.25–0.50), Good (0.5–0.80), Acceptable (0.80–0.94). ** Acceptable (0.15–0.20), Good (0.2–0.69), Very good (0.70–0.95), Excellent (0.95–1). *** A value of 1 represents a perfect regular element. **** Acceptable (<35) depending on mesh configuration. † Optimized reactor design with a gap distance of 5 mm.

2.3.3. Characterization of Materials and Macroscopic-Phase Reactions

Ansys Fluent contains a database of material properties that were integrated into the simulation. The consumption (Hacac, BDEAS, and O_3) and generation (H_2O, DEA, and O_2) of various species require the specification of thermodynamic properties to simulate the macroscopic behavior through computational fluid dynamics. However, some thermodynamic properties of the reagents, including Hacac and BDEAS, are limited in literature and experimental data; thus, ab initio quantum mechanics simulations are performed to compute the thermophysical parameters (enthalpy of formation, entropy of formation, specific heat at constant pressure) for materials with insufficient data. Quantum ESPRESSO contains programs dedicated to evaluating material properties using density functional theory (DFT) in conjunction with the Quasi Harmonic Approximation (QHA), which is integrated to evaluate the material properties. The computed thermophysical properties were cross-validated with literature results for some properties via the National Institute of Standards and Technology (NIST) database for Hacac and by comparison to similar molecules such as bis(dimethylamino)silane (BDMAS) for BDEAS. Additionally, properties including the thermal conductivity and the viscosities were also defined to each gaseous species. The thermal conductivities of each gas-phase species were approximated to that of air, which is composed of nitrogen and oxygen gas, and is similar to the composition of the species in the reactor. The viscosities of each for species not available in the Ansys Fluent database were obtained through material safety data sheets (MSDS) available online. As summarized in Table 2, these thermophysical properties are then defined into the macroscopic simulation on Ansys Fluent for a reference temperature of 273 K.

Table 2. Thermophysical material properties of species specified in the gas phase in Ansys Fluent.

Thermophysical Parameter	Hacac	BDEAS	DEA
Standard Enthalpy of Formation [J/kmol]	-3.844×10^8	-6.484×10^8	-7.25×10^7
Standard Entropy of Formation [J/kmol·K]	-3.502×10^5	5.338×10^3	-4.845×10^5
Specific Heat [J/kg·K]	208.2	Polynomial [†]	Polynomial [†]
Thermal Conductivity [†] [W/m·K]	0.0100	0.0100	0.02
Viscosity [†] [kg/(m·s)]	6.00×10^{-4}	1.10×10^{-2}	3.19×10^{-4}

[†] Obtained from NIST or MSDS references. Other parameters were calculated from Quantum ESPRESSO.

In the reactor configuration, highly pure ozone is generated from an ozone-enriched source, which is available in industry [62]. Therefore, it is assumed that ozone is obtained by liquid ozone from an ozone generator and fed to spatial reactors through the O_3 injection port. However, as an oxidizing agent, ozone is used in Step C, which is capable of decomposing in the fluid phase at high operating temperatures in a mechanism that was first proposed in 1957 [63]. Thus, it is important to account for this thermal decomposition of ozone, which is a highly unstable molecule, in the macroscopic CFD simulation.

$$O_3 \rightleftharpoons O_2 + 2O$$

$$O + O_3 \rightarrow O_2$$
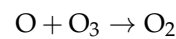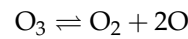
Apart from the surface kinetics established by the mesoscopic model, the volumetric reactions from the ozone decomposition are directly defined in the macroscopic model. All kinetic parameters for the decomposition of ozone were determined by [63]. The consumption of O_3 and generation of O_2 are calculated and included in the mass balance equation for ozone in Equation (8).

2.3.4. Numerical Solution Methods

The mass, momentum, and energy conservation equations are solved in the CFD simulation as described below:

$$\frac{\partial \rho}{\partial t} + \nabla \cdot (\rho \overrightarrow{v}) = S_m \tag{8}$$

$$\frac{\partial (\rho \overrightarrow{v})}{\partial t} + \nabla \cdot (\rho \overrightarrow{v} \overrightarrow{v}) = -\nabla p + \nabla \cdot (\overline{\overline{\tau}}) + \rho \overrightarrow{g} + \overrightarrow{F} \tag{9}$$

$$\frac{\partial}{\partial t} (\rho E) + \nabla (\overrightarrow{v} (\rho E + p)) = -\nabla (\Sigma h_j J_j) + S_h \tag{10}$$

where ρ represents the density of the fluid composition, $\overrightarrow{v}$ is the velocity of the fluid mixture, S_m denotes the rate of species generation or consumption source term, p is the static pressure of the fluid, $\overline{\overline{\tau}}$ corresponds to the symmetric rank-two stress tensor, $\overrightarrow{g}$ is the gravitational acceleration constant, $\overrightarrow{F}$ is the external body force, E is the internal energy of the system, h_j symbolizes the sensible enthalpy of species j, J_j represents the diffusion flux of species j, and S_h denotes the heat flux source rate term. Spatiotemporal numerical solutions for each node in the mesh are computed with the pressure-based coupled solver provided by Ansys Fluent, which simultaneously solves the mass and momentum continuity equations, Equations (8) and (9), with greater computational efficiency and convergence speed compared to the segregated pressure-based solver approach. To model the temporal dynamics, a transient solver method is proposed by adopting a first-order implicit formulation with a fixed 0.001 s time interval. Although higher order methods could have been employed to reduce the global error induced from the numerical method, the first-order implicit method was chosen to lessen the overall computation time of the process while preserving convergence criteria. Lastly, the Gauss-Seidel iterative method is utilized to solve algebraic systems by default.

2.3.5. Simulation Modeling

Several features are defined to reduce the degrees of freedom by specifying boundary conditions and fluid flow conditions. No-slip and zero diffusion flux boundary conditions are defined to the reactor walls for simplicity and surface of the substrate to resemble the self-limiting behavior of the ASALD process. Various in silico modeling works [64–66] have assumed laminar flow conditions, which are applicable in industry [67]. However, notable disadvantages [68] of laminar flow conditions are irrelevant to this study due to the substrate being small in diameter (200 mm, in Section 2.3.2) and the reactor design is modeled to limit depleted reagents along the perimeter of the reaction zones.

The most notable advantage of Ansys Fluent is its high versatility in the form of User-Defined Functions (UDFs). A UDF is a function that is able to enhance CFD simulations by customizing boundary conditions, defining material properties, and even initializing simulations, for instance. In this study, several UDFs are utilized to define mass flow rates and reagent mole fractions, source terms for species generation and consumption, temperature, the motion of the wafers with respect to the reactor, and allocating indexes in User-Defined Memories (UDMs). UDMs allow Ansys Fluent to find the appropriate nodes for computing reagent consumption and byproduct generation. Additionally, wafers are radially sliced into 10 equiangular sections so that mesoscopic simulations are executed in parallel, as shown in Figure 6. Thus, 10 mesoscopic simulations are conducted on each wafer, and the coverage on the 10 sections of a wafer from the mesoscopic simulation is computed as an area-weighted average. Given that 3 wafers are equipped in a spatial reactor, 30 UDMs must be applied to specify the nodes in which the consumption and generation of species take place.

Due to the versatility and advantages mentioned in Section 1 of numerical multi-physics modeling, computational fluid dynamics studies are broadly applied for industrial processes under various operating conditions. However, the computation efficiency (e.g., computational burden and time) heavily relies on computing resources. For example, to reduce numerical errors, high-order numerical methods with extremely fine meshes increase computing costs. Therefore, appropriate size of the mesh elements and numerical methods should be employed. In this study, 36-core dual processors with 384 GB of RAM (Random-Access Memory) are utilized to simulate the multiscale CFD model.
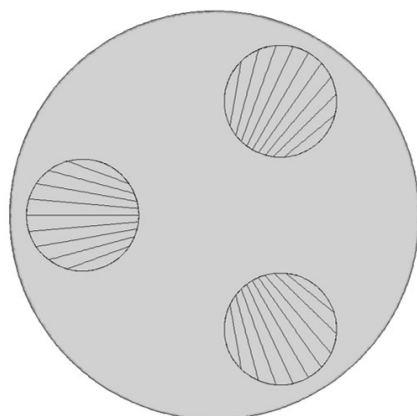

Figure 6. Three wafers on the rotating plate. Each wafer has 10 equiangular sections to evaluate 10 surface area-averaged pressures to evaluate an averaged surface coverage, and source generation and consumption rates.

3. Results and Discussion

3.1. Reactor Optimization

In the design of the reactors for ABC-ASALD processes, the most important criterion considered is the film uniformity, as it is directly related to the quality of semiconductor chips. A reactor with high film uniformity guarantees precise control over the thickness of

deposition films when constructing 3D features on nanochips. When discussing film uniformity, there are several other factors that may be evaluated with a more rapid turnaround time than directly measuring film uniformity, such as the reagent exposure time distribution of the substrate and whether there is any intermixing present.

3.1.1. Exposure Time Distribution

The exposure time is defined as the amount of time that a section of the substrate is exposed to the reagents. Depending on reactor geometry and design, the exposure time may vary across the surface of the wafer. Thus, it is vital to examine the distribution of exposure times for various reactors and ensure a tight distribution of exposure times. For a spatial reactor, the exposure time for a specific point is determined not by the gas distribution device, but rather by the shape of the reaction zones where the substrate enters by the rotation of the bottom plate. To investigate the effect that reaction zone configurations have on the exposure time distribution, steady-state and dynamic simulations of **R1**, which has circular reaction zones, and **R4**, which has annular-sectioned reaction zones, were performed with a reactant mole fraction of 0.1 and with an angular velocity of 0.8 rad/s. The results are displayed in Figure 7.
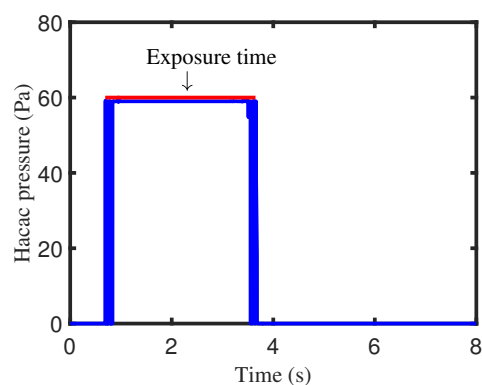

Figure 7. Hacac partial pressure over time on a node in the mesh. As the wafer rotates, the pressure rises around 0.8 s to reach the plateau and goes to 0 around 3.6 s. The length of the straight line in red is defined as the exposure time.

To evaluate the exposure time distribution for Hacac, the partial pressure of Hacac was recorded at every node of the meshed wafer surface as it traveled through the Hacac reaction zone. This data was then used to determine how long each wafer node spent saturated with Hacac, which is the exposure time. After being processed, all the nodal data was plotted in Figure 8c,d, and the wafer surface contours for all nodes are shown in Figure 8a,b. Results suggest that the geometry of the reaction zones for **R1** and **R4**, which are presented in Figure 5a,d, respectively, directly affect the distribution of nodal exposure time.

From a physical standpoint, the exposure time distribution is expected to exhibit low variance when all the nodes on the moving wafer experience the same amount of time in the reaction zone. However, the proposed circular spatial reactor differs from a linear sheet-to-sheet reactor in that the wafers are rotating in an angular fashion around the reactor, causing the edge of the wafer that is furthest from the center of the reactor to be traveling at a faster tangential velocity. Thus, to ensure that each point of the wafer spends the same amount of time in the reaction zone, the ideal reaction zone shape must consist of arc lengths that are solely dependent on their radial distance from the center of the reactor. This condition is best fulfilled by the annular-sectioned reaction zones of reactor **R4**. For reactor **R1**, however, the central region of the substrate is expected to have longer exposure times compared to that of the outer region of the substrate due to the round reaction zone, which is easily demonstrated by examining the point on the wafer that is the furthest from the center of the reactor. This point will only be present in the reaction zone for a short time

as the arc length of the reaction zone at that radius is small; thus, all sections of the wafer will not be exposed at the same time.

As illustrated in Figure 8c, the bar chart for **R1** shows that the reactor has a wide exposure time distribution, especially when compared to the tightly centered exposure time distribution of **R4**, whose bar chart is found in Figure 8d. While the average exposure time for both reactors is around 2.7 s, with **R1** having an average exposure time of 2.717 s and **R4** having an average exposure time of 2.701 s, the two vary greatly in terms of the standard deviation; the standard deviation of **R1** and **R4** were computed as 0.1925 and 0.0079, respectively. This large difference in standard deviation between the two reactors aligns with the predicted result, and it demonstrates that the standard deviation of the exposure times on the wafer is directly correlated to the shape of the reaction zones. To produce films with high uniformity, the reactor must have reaction zones shaped like annular sections as shown in **R4**.
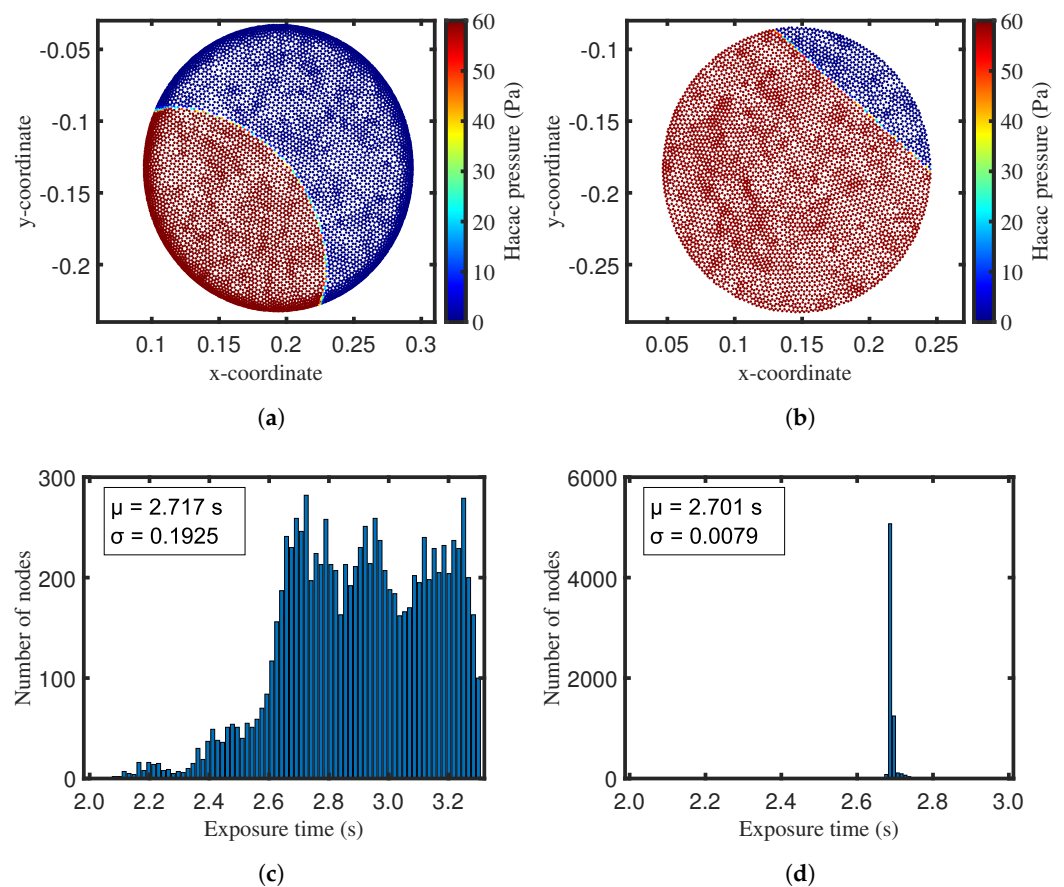

(a)

(b)

(c)

(d)

Figure 8. Hacac pressure contours across the wafer in (**a**) **R1** at 2 s and (**b**) **R4** at 3 s. The red region in (**a**,**b**) indicates the area that is covered with the reagent, Hacac. Distribution of exposure time for all nodes in the wafer for (**c**) **R1** and (**d**) **R4**. μ and σ represent the average and standard deviation, respectively. There are 10,410 nodes in **R1** and 6737 nodes in **R4**.

3.1.2. Intermixing

The uniformity of the film produced by a spatial reactor is not solely dependent on the exposure time distribution and the shape of the reactor zones. Another crucial factor is the gas distribution across the reaction and purge zones. A nonuniform gas distribution causes the residence time of the reagents across the wafer to vary, which prevents the reactor from achieving optimal surface coverage and high film uniformity [67]. Inside spatial reactors, reagents are successfully separated from the reaction zone by the injection of N_2 gas, thereby establishing a boundary layer that prevents the diffusion of the reagents into the purging region by convection. As the gas flow inside the reactor is assumed to be

laminar in Section 2.3, nonuniform gas distribution mainly occurs when reactants cross into the purge zones. This phenomenon is named intermixing, and preventing it is vital to ensure uniform film growth. Intermixing is mainly caused by the substrate physically dragging unreacted reactants into the purge zone, which means that it is correlated to three features of reactor design: the gap distance, the wafer velocity, and the vacuum pressure. As intermixing is a binary criterion in that it is either present or is not, it is best to first determine the domain in which no intermixing is present before identifying other criteria such as fastest computational speed or fastest processing speed to select the optimal reactor design.

The gap distance is defined as the distance separating the wafer and the gas distribution assembly, and it is one of the most important factors in effectuating self-limiting behavior and minimizing reagent intermixing. In this work, the effects of gap distance on intermixing was studied with **R2** at different gap distances of 10 mm, 5 mm, and 1 mm. As shown by N_2 mole fraction contours in Figure 9, a lower gap distance inhibits reagent intermixing in the purging regions. This observation of how gap distance affects intermixing has been explored in several works for different spatial reactor configurations [40,41].
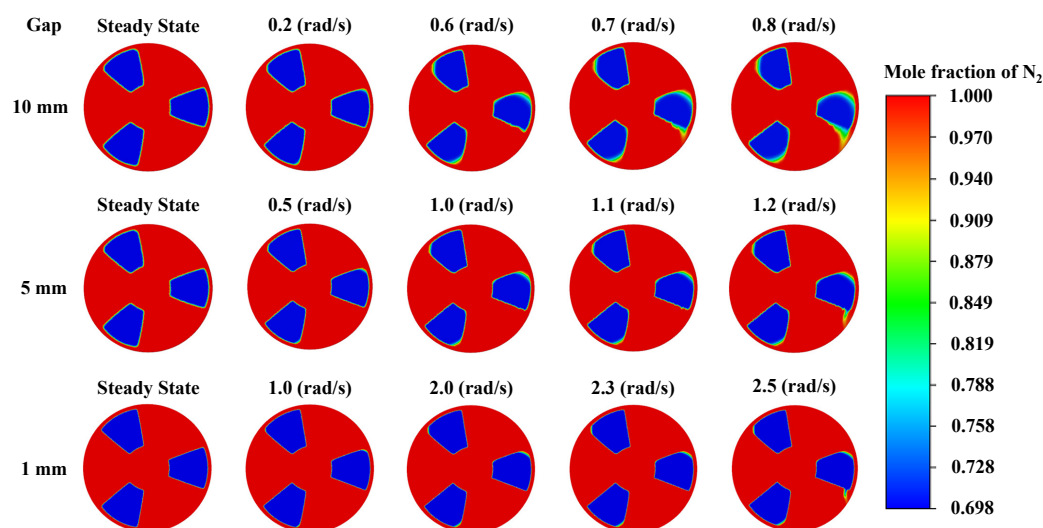

Figure 9. Contours of the mole fraction of nitrogen on the plate rotating clockwise in **R2** with gap distances of 10 mm, 5 mm, and 1 mm in various angular velocities, which depict the invasion of N_2 into the reaction zones and reagent runoff into the purge zones at higher rotation speeds.

However, despite lower gap distances reducing the intermixing of reagents, a higher number of discretized elements are needed to resolve boundary layers around separating chambers to ensure the accuracy of the numerical model, which carries greater computational burden. Thus, this study will account for a balance in the computational efficiency of the multiscale simulation and effective reagent separation. For the aforementioned reasons, a 5-mm gap distance is integrated into the idealized reactor configuration.

The wafer velocity also affects the intermixing of reagents. Greater angular velocities were observed to increase intermixing in response to the push of reagents in the direction of the angular rotation of the wafer. Both Figures 9 and 10 show how the N_2 mole fraction contours change with the angular wafer velocity. Figure 10 in particular, reveals that the invasion of the inert gas (denoted by the ring in orange) at the entry of the reaction zone and the reagent runoff (denoted by the ring in green) at the exit are both conveyed in the direction of the wafer rotation (counter-clockwise). Thus, these instances of intermixing are attributed to the motion of the wafer. As shown in Figure 9, with a 5-mm gap distance, the inert gas of N_2 is observed to enter the reaction zone when the angular wafer velocity is above 1.0 rad/s. The reagent enters the purge zone when the angular wafer velocity

is above 1.2 rad/s. Thus, to maintain a self-limiting reaction with no intermixing, the rotation speed must be kept below 1.0 rad/s. Thus, it is imperative to construct a reactor configuration that handles sufficiently high angular velocities to reduce process time while simultaneously producing uniform deposition and promoting effective reagent separation.

To establish effective gas separation and an acceptable process time, it is essential to choose an appropriate rotation speed and gap distance to achieve precise thin film thickness control and surface uniformity. While lower gap distances minimize the effects of reagent intermixing, several operating and reactor design conditions are also considered for minimizing the intermixing of reagents. Thus, an effective balance between the gap distance, (selected to be 5 mm), the vacuum pressure (chosen to be -150 Pa), and the orientation (symmetrical or asymmetrical) of the injection ports are methodically chosen to enable a higher range of substrate angular velocities to be used for the process. For instance, the reactor model **R3** repositions the cylindrical injection ports closer to the substrate entry in the reaction zone as shown in Figure 5c, which establishes an asymmetrical inlet configuration. The mole fraction contours of N_2 for reactor model **R3** in Figure 10 shows marginal improvement of intermixing, particularly in the reagent runoff from the reaction zone at 1.0 rad/s as opposed to that of **R2**, which was modeled with a symmetrical inlet arrangement. **R4** (as shown in Figure 5d), with annular sector-shaped reagent inlets, was proposed to further mitigate intermixing as shown in Figure 10. To be specific, the invasion of the inert gas into the reaction zone disappears at both 0.8 and 1.0 rad/s in contrast with **R2** and **R3**, which both still show signs of intermixing at those velocities. Therefore, **R4** is selected as the desired reactor configuration to explore the ASALD process to discuss the quantitative relationship between various operating conditions on the surface coverage in Section 3.2.
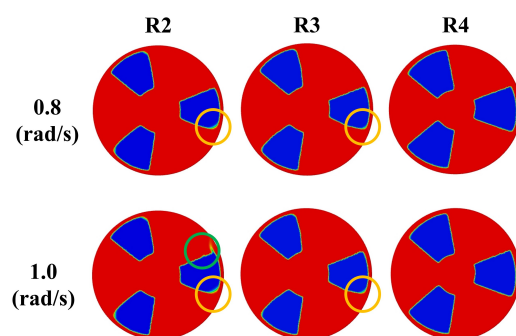

Figure 10. Contours of the mole fraction of nitrogen on the plate rotating clockwise in **R2**, **R3** and **R4** with a gap distance of 5 mm in the angular velocities of 0.8 and 1.0 rad/s. The legend for the contours is present in Figure 9. A ring in orange denotes a nitrogen invasion into the BDEAS reaction zone, and a ring in green denotes the BDEAS runoff from the reaction zone.

3.2. Multiscale Simulation Results

The reactor optimization study examines the impact that the gap distance, the injection and outlet port geometry, and the wafer angular velocity have on reagent separation, exposure time distribution, reagent distribution on the substrate surface, and computational efficiency. After considering all the above criteria, reactor model **R4** was designed with a 5-mm gap distance. The next component of this work will examine the effects that operating conditions such as wafer velocity and reagent mole fractions have on the surface coverage for Steps A, B, and C.

The simulations were conducted with a range of rotation speeds, ω, (0.2 rad/s $\leq \omega \leq$ 0.8 rad/s) and a range of reactant species mole fraction, x (0.05 $\leq x \leq$ 0.70) to determine optimal operating conditions to achieve complete surface coverage. For all steps, the surface coverage depends on the rotation speeds and the mole fractions of the reactant species, as illustrated in Figure 11. In general, the coverage for each step increases as the mole fraction of the reactant species increases and as the rotation speed decreases. An increase in the

mole fraction of the reactant species naturally leads to an increase in the partial pressure of the species, which accelerates the reaction rates for all adsorption reactions according to Collision Theory. Furthermore, a lower rotation speed allows the wafer to be exposed to the reagent for a longer period of time, thus increasing the surface coverage. Specifically, the Hacac step reaches full coverage at 0.2 rad/s with Hacac mole fractions of $x_{Hacac} = 0.05$, 0.1, and 0.3. However, the coverage decreases with increasing rotation speed. At 0.6 rad/s, full coverage is only achieved with $x_{Hacac} = 0.3$; for lower Hacac mole fractions, surface coverages of 98.8% and 95.1% were observed. BDEAS and ozone coverage curves also reveal a similar trend. However, the curves for BDEAS appear discontinuous, which is attributed to its proposed kinetic mechanism. An observable limitation of the kMC method is that the algorithm requires a priori knowledge of a reaction mechanism [69] that, if exceedingly simplified, will reduce the accuracy of the kMC model when trying to predict realistic surface kinetics. Figure 11b exemplifies a noncompetitive BDEAS adsorption in which desorption and intermediate pathways are not immediately observed after the adsorption reaction takes place. This work utilized a kinetics mechanism determined by [33] with large activation energy differences that were evaluated using the nudged elastic band method by [34]. Such reaction mechanism introduces a spontaneous reaction path where the surface coverage is dictated by the large reaction rate constant differences that generate this noncompetitive kinetics mechanism, where one reaction path dominates. Additionally, the repulsive forces due to the steric effects reduced the versatility of pursuing intermediate or reverse reaction paths, therefore, producing steeper coverage curves.
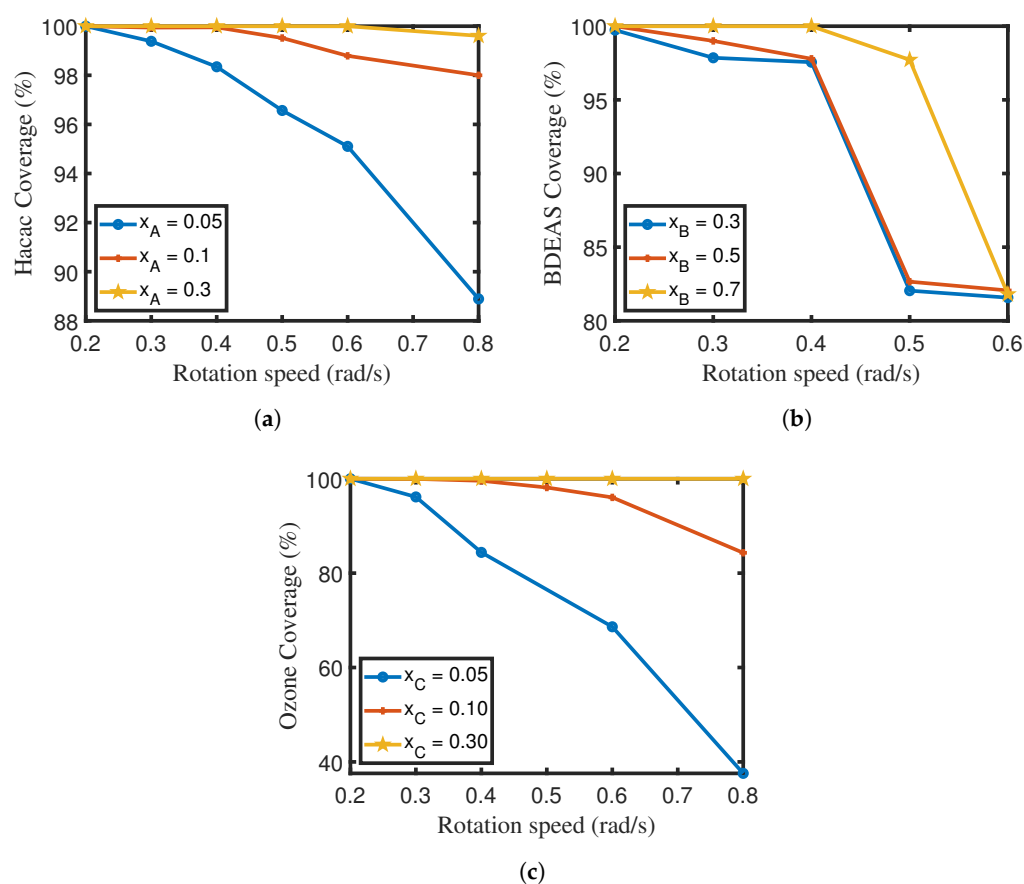

(a)

(b)

(c)

Figure 11. Coverage (%) versus rotation speed (*rad/s*) for (**a**) Hacac step, (**b**) BDEAS step, and (**c**) ozone step. x_A, x_B, and x_C represents the mole fraction of Hacac, BDEAS, and ozone, respectively.

Noncompetitive kinetics offer insight to the discontinuous curves presented in Figure 11; however, the mole fraction gradient along the boundary between the purging and reaction zone presents a challenge for collecting pertinent surface pressure data that will capture

the initial adsorption step for smaller time and length scales. This concentration gradient is presented in Figure 12, which illustrates the lack of nodal data due to the small length scales required to collect additional pressure data. Additionally, at higher angular velocities, the collection of nodal data becomes more challenging due to this small boundary length scale (in μm), which is another reason for the discontinuous curves generated in Figure 11. Consequently, the smaller length scale in micrometers would require smaller time scales (milliseconds) to collect surface coverage data within this boundary layer, as illustrated in Figure 2. Thus, the spatiotemporal progression of coverage of the wafer surface would be more difficult to simulate at the reaction zone entrances.
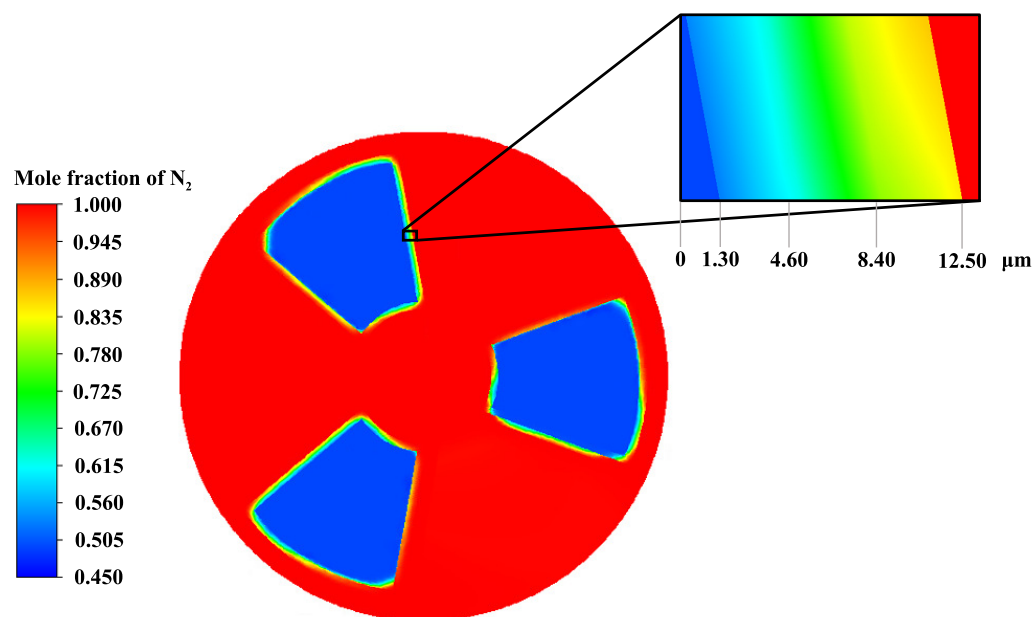

Figure 12. Concentration gradient of N_2 mole fraction for **R4** illustrating the small length scales in micrometers for each contour along the reagent-purge boundary region, which limits the availability for studying the temporal progression of surface coverage as depicted in Figure 2.

When comparing the multiscale CFD simulation process times to reach full coverage compared to that of the mesoscopic model from prior work [34], the multiscale CFD simulation process times were slower. The integration of the macroscopic model to the mesoscopic model introduced pressure depletion zones that diluted the surface exposure to reagents, thereby reducing the adsorption reaction rates for Hacac and BDEAS. For a constant temperature of 523 K and constant Hacac surface pressure of 130 Pa (Step A), a constant BDEAS surface pressure of 400 Pa (Step B), and a constant O_3 pressure of 130 Pa (Step C), the mesoscopic simulation evaluated complete coverage times of 2.29 s, 2.28 s, and 3.81 s, respectively [34]. The multiscale CFD simulation results with similar reactor operating conditions require process times of 3.77 s, 6.99 s, and 3.72 s to achieve full coverage for Steps A, B, and C, respectively as illustrated in Figure 13. The integration of macroscopic fluid behavior with the mesoscopic model indicates that the reagent depletion zones and repulsions generated by species intercollisions in the fluid phase contribute to the substantial increase in the process times, which was observed from a prior multiscale modeling work [70]. However, the proposed model, which partitions the wafer into 10 sections and performs 10 kMC simulations on each section, inaccurately characterizes the surface coverage progression as a function of time. Ideally, a kMC simulation for each node on the wafer surface would greatly improve the accuracy of the times to obtain complete surface coverage, but comes at a computational cost. However, the results are consistent with experimental findings where Hacac dosage times of 5 s in similar operating conditions were used to ensure complete surface coverage [9]. Additionally, BDEAS dosage times of 6 s were employed to maximize the deposition thickness of the SiO_2 surface [33],

although, greater dosage times were observed to contribute to the nucleation of the oxide film if BDEAS is oversaturated in the reactor. To prevent such a scenario, the rotary reactor design evacuates unreacted reagent through the purge streams, thereby maintaining the operating pressure of the reagent within the reaction zone. Lastly, O_3 dosage times of 2.5 s to 20 s to achieve complete surface coverage [71], which is analogous to the multiscale computed time.
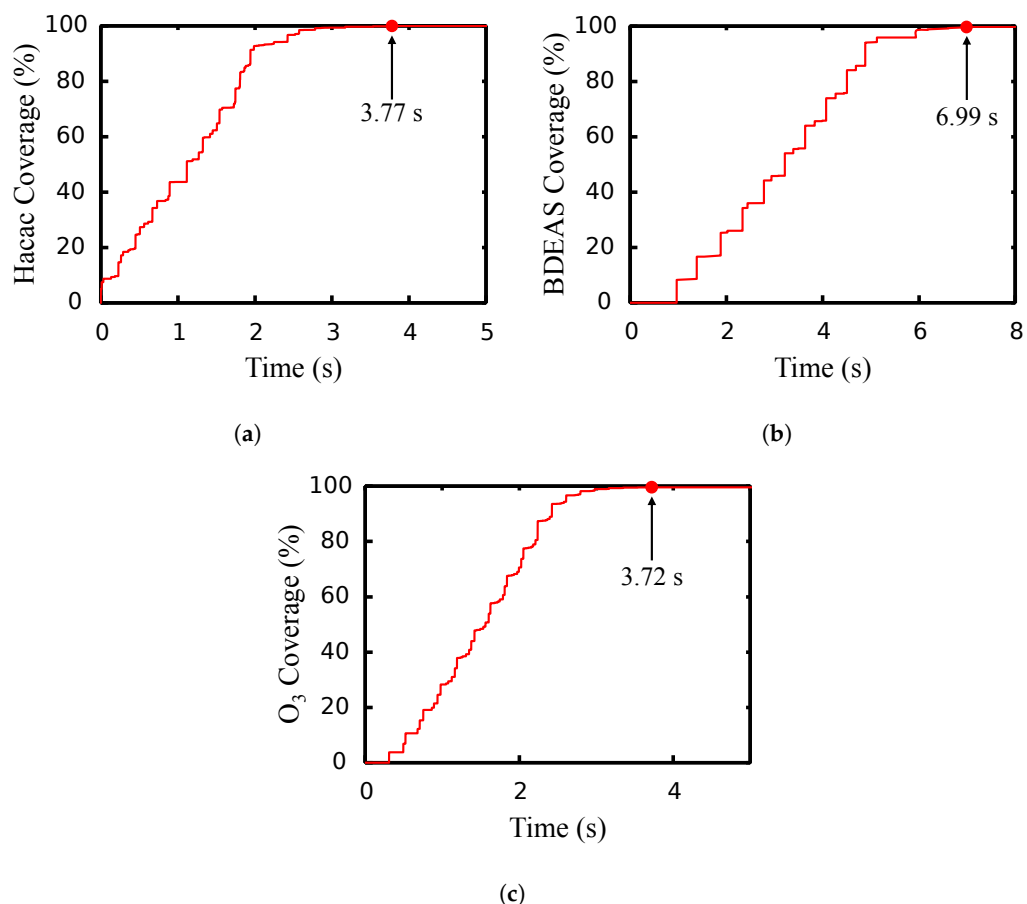

Figure 13. Multiscale CFD plots illustrating the surface coverage (%) progression as a function of time for (**a**) 0.1 mole fraction Hacac adsorption, (**b**) 0.5 mole fraction BDEAS adsorption, (**c**) 0.1 mole fraction O_3 adsorption. Evaluated multiscale process times to reach full surface coverage were longer than observed mesoscopic model process times conducted from prior work [34].

Figure 14 illustrates the contours of species mole fractions simulated with a constant rotation speed of 0.4 rad/s and a mole fraction of 0.3 for Hacac, BDEAS, and ozone. Due to the fixed rotation speed imposed to the three wafers, the equal areas of each wafer are exposed to each reagent as shown in Figure 14a. However, the reaction progression for each reaction, which is inspected by measuring the generation of byproducts from the wafer surface, is different as revealed in Figure 14b–d. As discussed above, BDEAS adsorption requires higher mole fraction and lower rotation speeds to achieve complete coverage compared with Hacac and ozone adsorption. Despite the fact that more than half of the wafer area is in the BDEAS-enriched reaction zone (in Figure 14c), the byproduct, DEA, is only observed in a small area, which is the area that first encountered the reagent due to the BDEAS adsorption mechanism, and the steric effects discussed in Section 2.2. Meanwhile, H_2O produced from Hacac adsorption and O_2 produced from O_3 adsorption are being generated on the region closer to the boundary between the reagent and the inert gas. In other words, Step A and Step C are faster than Step B, which is in agreement with ab initio DFT calculation results [34,50,72] where the BDEAS adsorption undergoes multiple steps that have higher activation energies than Hacac and ozone. Therefore, the mole fractions

of reactants must be carefully selected to optimize the process. When selecting operating conditions, the BDEAS and Ozone steps can be firstly considered since Hacac is covered on the non-growth area at the first cycle and afterward, only the deprived reaction sites are refilled and reinforced. From the multiscale simulations, the mole fractions of 0.1, 0.5, and 0.1 for Hacac, BDEAS, and O_3, respectively, and a rotation speed of 0.2 rad/s can be considered as an optimal operating condition for full coverage.
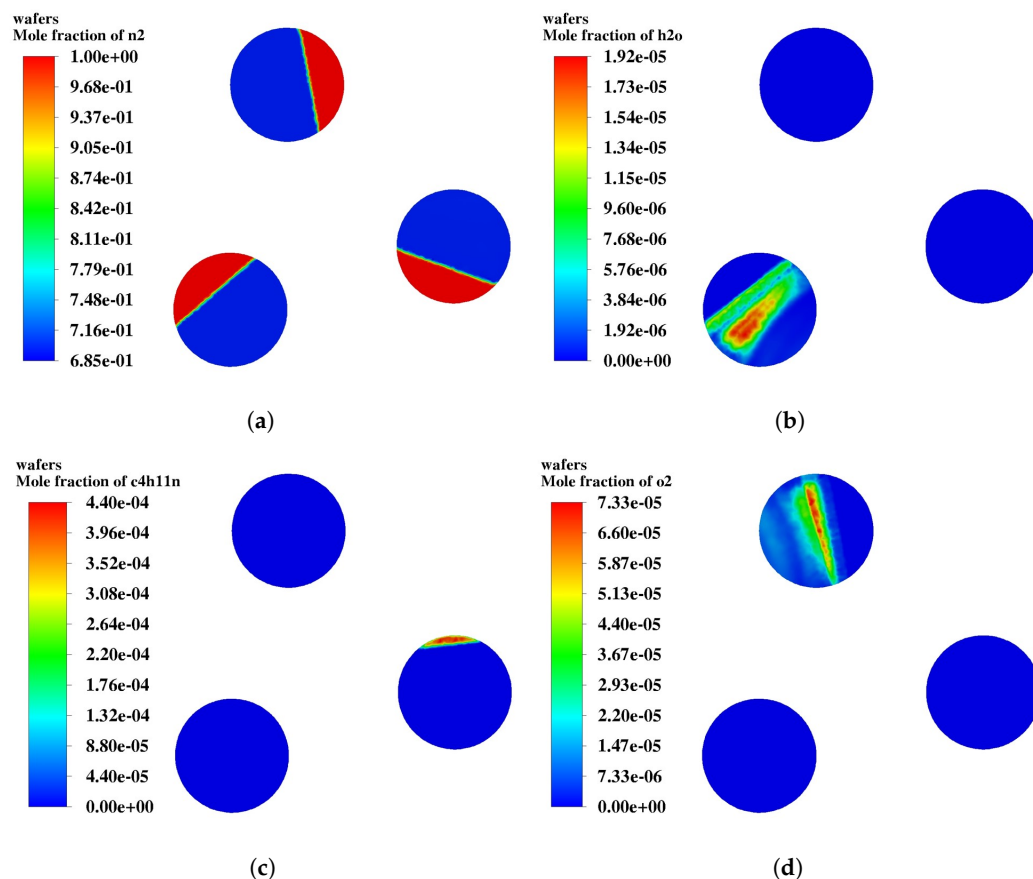

Figure 14. Contours of (**a**) Nitrogen mole fraction, (**b**) H_2O mole fraction, (**c**) DEA mole fraction, and (**d**) O_2 mole fraction on the wafers at 2 s with 0.4 rad/s From bottom left counter-clockwise, the wafers in the Hacac, BDEAS, and ozone reaction zones, respectively.

4. Conclusions

An in silico multiscale computational fluid dynamics model was developed for an area-selective atomic layer deposition (ASALD) process on the substrate of SiO_2/Al_2O_3 utilizing a spatial reactor design. Three reagents were used to deposit SiO_2 thin films on the growth area (SiO_2) and to create protective layers on the nongrowth area (Al_2O_3): the inhibitor (acetylacetone or Hacac), precursor (bis(diethylamino)silane or BDEAS), and oxidant (ozone) for Steps A through C, respectively. This model included an atomistic-mesoscopic model using kinetic Monte Carlo (kMC) and a macroscopic model using computational fluid dynamics (CFD). Foremost, a spatial reactor configuration was optimized to ensure uniform reagent exposure time distribution and effective reagent separation to ensure self-limiting behavior was maintained. The gap distance, rotation speed, and reactor geometries were observed to have great influence on transport behavior of gas species. Lower gap distances and rotational speeds are required to avoid reagent intermixing. In addition, a ring, sector-shaped outlet and N_2 inlet improved reagent separation by removing the reagent runoff and inert invasion; thus creating a low variance gas distribution, leading to uniform exposure to reagents. A more uniform flow was observed with asymmetrical, annular, sector-shaped reagent inlets. After an optimal reactor configuration was built, the

multiscale model was simulated within the operating range of $0.2 \, \mathrm{rad/s} \leq \omega \leq 0.8 \, \mathrm{rad/s}$ with different mole fractions of species for Hacac, BDEAS, and ozone. Sufficiently low angular speeds were required for complete surface deposition by providing longer exposure time to the reagents. A higher mole fraction of species also accelerated the adsorption reactions to reach complete coverage.

It is essential to choose an appropriate mole fraction of each reagent, since all reaction zones rotate at the same velocity. Since the BDEAS reaction takes longer time, a higher mole fraction for BDEAS than the ones for Hacac and ozone is required to obtain full coverage at the same wafer rotation speed. Due to the advantage of this modeling study that can generate a broad set of data at varying operating conditions, this in silico work has the potential to expedite reaction scale-up in industry. Therefore, this modeling approach offers insights and data to process engineers to select proper operating conditions for further process development. On top of that, this study presents guidelines to design and optimize a rotary type spatial reactor in an industrial setting. Finally, as described in Section 1, further research is needed to design an optimal control system for robust process operation. Specifically, given the complexity of the reaction taking place inside these reactors, advanced control methods for ASALD (e.g., model predictive control, artificial neural network-based run-to-run control) can be developed in a future work to ensure robust process operation.

Author Contributions: Conceptualization, S.Y., H.W., M.T., F.O., G.O. and P.D.C.; methodology, S.Y., H.W., M.T., F.O., G.O. and P.D.C.; software, S. Y., H.W., M.T. and F.O.; validation, S. Y., H.W., M.T. and F.O.; formal analysis, S. Y., H.W., M.T. and F.O.; investigation, S. Y., H.W., M.T. and F.O.; resources, P.D.C.; data curation, S. Y., H.W., M.T. and F.O.; writing—original draft preparation, S. Y., M.T., H.W. and F.O.; writing—review and editing, S. Y., M.T., H.W., F.O., G.O. and P.D.C.; supervision, G.O. and P.D.C.; funding acquisition, P.D.C. All authors have read and agreed to the published version of the manuscript.

Institutional Review Board Statement: Not applicable.

Informed Consent Statement: Not applicable.

Data Availability Statement: All data will be available upon written request to the corresponding author.

Conflicts of Interest: The authors declare no conflict of interest.

Abbreviations

The following abbreviations are used in this manuscript:

ALD	Atomic layer deposition
ASALD	Area-selective atomic layer deposition
BDEAS	bis(diethylamino)silane
CFD	Computational fluid dynamics
DEA	diethylamine
DFT	Density functional theory
EPE	Edge placement error
Hacac	acetylacetone
kMC	Kinetic Monte Carlo
NEB	Nudged elastic band
NGA	Nongrowth area
SMI	Small-molecule inhibitor
UDF	User-defined function
UDM	User-defined memory

References

1. Wang, C.P.; Tsai, Y.P.; Lin, B.J.; Liang, Z.Y.; Chiu, P.W.; Shih, J.R.; Lin, C.J.; King, Y.C. On-Wafer FinFET-Based EUV/eBeam Detector Arrays for Advanced Lithography Processes. *IEEE Trans. Electron. Devices* **2020**, *67*, 2406–2413. [CrossRef]
2. Chen, M.C.; Li, K.S.; Li, L.J.; Lu, A.Y.; Li, M.Y.; Chang, Y.H.; Lin, C.H.; Chen, Y.J.; Hou, Y.F.; Chen, C.C.; et al. TMD FinFET with 4 nm thin body and back gate control for future low power technology. In Proceedings of the IEEE International Electron Devices Meeting, Washington, DC, USA, 7–9 December 2015; pp. 32.2.1–32.2.4.
3. Huang, J. Research Progresses on Suppressing the Short-Channel Effects of Field-Effect Transistor. *Highlights Sci. Eng. Technol.* **2022**, *27*, 361–367. [CrossRef]
4. Angelov, G.V.; Nikolov, D.N.; Hristov, M.H. Technology and Modeling of Nonclassical Transistor Devices. *J. Electr. Comput. Eng.* **2019**, *2019*, 4792461. [CrossRef]
5. Barraud, S.; Previtali, B.; Vizioz, C.; Hartmann, J.M.; Sturm, J.; Lassarre, J.; Perrot, C.; Rodriguez, P.; Loup, V.; Magalhaes-Lucas, A.; et al. 7-Levels-Stacked Nanosheet GAA Transistors for High Performance Computing. In Proceedings of the 2020 IEEE Symposium on VLSI Technology, Hsinchu, Taiwan, 10–13 August 2020; pp. 1–2.
6. Wang, S.; Liu, X.; Zhou, P. The Road for 2D Semiconductors in the Silicon Age. *Adv. Mater.* **2022**, *34*, 2106886. [CrossRef]
7. Bhattacharyya, K. Tough road ahead for device overlay and edge placement error. In *Proceedings of the Metrology, Inspection, and Process Control for Microlithography XXXIII*; Ukraintsev, V.A., Adan, O., Eds.; International Society for Optics and Photonics, SPIE: San Jose, CA, USA, 2019; Volume 10959, p. 1095902.
8. Mulkens, J.; Hanna, M.; Wei, H.; Vaenkatesan, V.; Megens, H.; Slotboom, D. Overlay and edge placement control strategies for the 7nm node using EUV and ArF lithography. In Proceedings of the Extreme Ultraviolet (EUV) Lithography VI, San Jose, CA, USA, 22–26 February 2015; Volume 9422, p. 94221Q.
9. Mameli, A.; Merkx, M.J.M.; Karasulu, B.; Roozeboom, F.; Kessels, W.E.M.M.; Mackus, A.J.M. Area-Selective Atomic Layer Deposition of SiO$_2$ Using Acetylacetone as a Chemoselective Inhibitor in an ABC-Type Cycle. *ACS Nano* **2017**, *11*, 9303–9311. [CrossRef]
10. Sharma, R.K.; Gupta, R.; Gupta, M.; Gupta, R.S. Dual-Material Double-Gate SOI n-MOSFET: Gate Misalignment Analysis. *IEEE Trans. Electron. Devices* **2009**, *56*, 1284–1291. [CrossRef]
11. Hobbs, R.G.; Petkov, N.; Holmes, J.D. Semiconductor Nanowire Fabrication by Bottom-Up and Top-Down Paradigms. *Chem. Mater.* **2012**, *24*, 1975–1991. [CrossRef]
12. Jasni, A.H. Chapter 5-Fabrication of nanostructures by physical techniques. In *Nanoscale Processing*; Thomas, S., Balakrishnan, P., Eds.; Elsevier: Amsterdam, The Netherlands, 2021; pp. 131–162.
13. Amadi, E.V.; Venkataraman, A.; Papadopoulos, C. Nanoscale self-assembly: Concepts, applications and challenges. *Nanotechnology* **2021**, *33*, 132001. [CrossRef]
14. Brummer, A.C.; Mohabir, A.T.; Aziz, D.; Filler, M.A.; Vogel, E.M. Fabrication and characterization of a self-aligned gate stack for electronics applications. *Appl. Phys. Lett.* **2021**, *119*, 142901. [CrossRef]
15. Yasmeen, S.; Ryu, S.W.; Lee, S.H.; Lee, H.B.R. Atomic Layer Deposition Beyond Thin Film Deposition Technology. *Adv. Mater. Technol.* **2022**, *8*, 2200876. [CrossRef]
16. Kinge, S.; Crego-Calama, M.; Reinhoudt, D.N. Self-Assembling Nanoparticles at Surfaces and Interfaces. *ChemPhysChem* **2008**, *9*, 20–42. [CrossRef]
17. Bae, C.; Shin, H.; Nielsch, K. Surface modification and fabrication of 3D nanostructures by atomic layer deposition. *MRS Bull.* **2011**, *36*, 887–897. [CrossRef]
18. Liu, T.L.; Bent, S.F. Area-Selective Atomic Layer Deposition on Chemically Similar Materials: Achieving Selectivity on Oxide/Oxide Patterns. *Chem. Mater.* **2021**, *33*, 513–523. [CrossRef]
19. Okasha, S.; Harada, Y. Atomic layer deposition of self-assembled aluminum nanoparticles using dimethylethylamine alane as precursor and trimethylaluminum as an initiator. *J. Nanoparticle Res.* **2022**, *24*, 242. [CrossRef]
20. Hayden, O.; Agarwal, R.; Lu, W. Semiconductor nanowire devices. *Nano Today* **2008**, *3*, 12–22. [CrossRef]
21. Barth, S.; Hernandez-Ramirez, F.; Holmes, J.D.; Romano-Rodriguez, A. Synthesis and applications of one-dimensional semiconductors. *Prog. Mater. Sci.* **2010**, *55*, 563–627. [CrossRef]
22. Guerfi, Y.; Larrieu, G. Vertical Silicon Nanowire Field Effect Transistors with Nanoscale Gate-All-Around. *Nanoscale Res. Lett.* **2016**, *11*, 210. [CrossRef]
23. Yang, P.; Yan, R.; Fardy, M. Semiconductor Nanowire: What's Next? *Nano Lett.* **2010**, *10*, 1529–1536. [CrossRef]
24. Fernández-Garrido, S.; Auzelle, T.; Lähnemann, J.; Wimmer, K.; Tahraoui, A.; Brandt, O. Top-down fabrication of ordered arrays of GaN nanowires by selective area sublimation. *Nanoscale Adv.* **2019**, *1*, 1893–1900. [CrossRef]
25. Seo, S.; Yeo, B.C.; Han, S.S.; Yoon, C.M.; Yang, J.Y.; Yoon, J.; Yoo, C.; Kim, H.-j.; Lee, Y.-b.; Lee, S.J.; et al. Reaction Mechanism of Area-Selective Atomic Layer Deposition for Al$_2$O$_3$ Nanopatterns. *ACS Appl. Mater. Interfaces* **2017**, *9*, 41607–41617. [CrossRef]
26. Fang, M.; Ho, J.C. Area-Selective Atomic Layer Deposition: Conformal Coating, Subnanometer Thickness Control, and Smart Positioning. *ACS Nano* **2015**, *9*, 8651–8654. [CrossRef]
27. Mullen, E.; Morris, M.A. Green Nanofabrication Opportunities in the Semiconductor Industry: A Life Cycle Perspective. *Nanomaterials* **2021**, *11*, 1085. [CrossRef]
28. Chen, R.; Kim, H.; McIntyre, P.C.; Porter, D.W.; Bent, S.F. Achieving area-selective atomic layer deposition on patterned substrates by selective surface modification. *Appl. Phys. Lett.* **2005**, *86*, 191910. [CrossRef]

29. Mackus, A.J.M.; Merkx, M.J.M.; Kessels, W.M.M. From the Bottom-Up: Toward Area-Selective Atomic Layer Deposition with High Selectivity. *Chem. Mater.* **2019**, *31*, 2–12. [CrossRef]

30. Huang, J.; Lee, M.; Lucero, A.; Cheng, L.; Kim, J. Area-Selective ALD of TiO$_2$ Nanolines with Electron-Beam Lithography. *J. Phys. Chem. C* **2014**, *118*, 23306–23312. [CrossRef]

31. Sinha, A.; Hess, D.W.; Henderson, C.L. Area selective atomic layer deposition of titanium dioxide: Effect of precursor chemistry. *J. Vac. Sci. Technol. B Microelectron. Nanometer Struct. Process. Meas. Phenom.* **2006**, *24*, 2523–2532. [CrossRef]

32. Merkx, M.J.M.; Angelidis, A.; Mameli, A.; Li, J.; Lemaire, P.C.; Sharma, K.; Hausmann, D.M.; Kessels, W.M.M.; Sandoval, T.E.; Mackus, A.J.M. Relation between Reactive Surface Sites and Precursor Choice for Area-Selective Atomic Layer Deposition Using Small Molecule Inhibitors. *J. Phys. Chem. C* **2022**, *126*, 4845–4853. [CrossRef]

33. Merkx, M.J.M.; Sandoval, T.E.; Hausmann, D.M.; Kessels, W.M.M.; Mackus, A.J.M. Mechanism of Precursor Blocking by Acetylacetone Inhibitor Molecules during Area-Selective Atomic Layer Deposition of SiO$_2$. *Chem. Mater.* **2020**, *32*, 3335–3345. [CrossRef]

34. Yun, S.; Ou, F.; Wang, H.; Tom, M.; Orkoulas, G.; Christofides, P.D. Atomistic-mesoscopic modeling of area-selective thermal atomic layer deposition. *Chem. Eng. Res. Des.* **2022**, *188*, 271–286. [CrossRef]

35. Poodt, P.; Cameron, D.C.; Dickey, E.; George, S.M.; Kuznetsov, V.; Parsons, G.N.; Roozeboom, F.; Sundaram, G.; Vermeer, A. Spatial atomic layer deposition: A route towards further industrialization of atomic layer deposition. *J. Vac. Sci. Technol. A* **2012**, *30*, 010802. [CrossRef]

36. Suntola, T.; Antson, J. Method for Producing Compound Thin Films. Google Patents 4,058,430A, 15 November 1977.

37. Freeman, D.C.; Levy, D.H.; Cowdery-Corvan, P.J. Process for depositing organic materials. Google Patents 7,858,144B2, 28 December 2010.

38. Sun, W.; Kim, Y.; Shin, J.; Yang, W. Shower head of Combinatorial Spatial Atomic Layer Deposition apparatus, Google Patents 20,170,025,417A, 2017.

39. Pan, D.; Jen, T.C.; Yuan, C. Effects of gap size, temperature and pumping pressure on the fluid dynamics and chemical kinetics of in-line spatial atomic layer deposition of Al$_2$O$_3$. *Int. J. Heat Mass Transf.* **2016**, *96*, 189–198. [CrossRef]

40. Cong, W.; Li, Z.; Cao, K.; Feng, G.; Chen, R. Transient analysis and process optimization of the spatial atomic layer deposition using the dynamic mesh method. *Chem. Eng. Sci.* **2020**, *217*, 115513. [CrossRef]

41. Li, Z.; Cao, K.; Li, X.; Chen, R. Computational fluid dynamics modeling of spatial atomic layer deposition on microgroove substrates. *Int. J. Heat Mass Transf.* **2021**, *181*, 121854. [CrossRef]

42. De la Huerta, C.M.; Nguyen, V.H.; Dedulle, J.M.; Bellet, D.; Jiménez, C.; Muñoz-Rojas, D. Influence of the Geometric Parameters on the Deposition Mode in Spatial Atomic Layer Deposition: A Novel approach to Area-Selective Deposition. *Coatings* **2018**, *9*, 5. [CrossRef]

43. Yun, S.; Tom, M.; Orkoulas, G.; Christofides, P.D. Multiscale Computational Fluid Dynamics Modeling of Spatial Thermal Atomic Layer Etching. *Comput. Chem. Eng.* **2022**, *163*, 107861. [CrossRef]

44. Tom, M.; Yun, S.; Wang, H.; Ou, F.; Orkoulas, G.; Christofides, P.D. Machine learning-based run-to-run control of a spatial thermal atomic layer etching reactor. *Comput. Chem. Eng.* **2022**, *168*, 108044. [CrossRef]

45. Poodt, P.; Lankhorst, A.; Roozeboom, F.; Spee, K.; Maas, D.; Vermeer, A. High-Speed Spatial Atomic-Layer Deposition of Aluminum Oxide Layers for Solar Cell Passivation. *Adv. Mater.* **2010**, *22*, 3564–3567. [CrossRef]

46. Sharma, K.; Hall, R.A.; George, S.M. Spatial atomic layer deposition on flexible substrates using a modular rotating cylinder reactor. *J. Vac. Sci. Technol. A* **2015**, *33*, 01A132. [CrossRef]

47. Poodt, P.; van Lieshout, J.; Illiberi, A.; Knaapen, R.; Roozeboom, F.; van Asten, A. On the kinetics of spatial atomic layer deposition. *JOurnal Vac. Sci. Technol. A* **2013**, *31*, 01A108. [CrossRef]

48. Maroudas, D. Multiscale modeling of hard materials: Challenges and opportunities for chemical engineering. *AIChE J.* **2000**, *46*, 878–882. [CrossRef]

49. Yun, S.; Tom, M.; Luo, J.; Orkoulas, G.; Christofides, P.D. Microscopic and Data-Driven Modeling and Operation of Thermal Atomic Layer Etching of Aluminum Oxide Thin Films. *Chem. Eng. Res. Des.* **2022**, *177*, 96–107. [CrossRef]

50. Roh, H.; Kim, H.L.; Khumaini, K.; Son, H.; Shin, D.; Lee, W.J. Effect of deposition temperature and surface reactions in atomic layer deposition of silicon oxide using Bis(diethylamino)silane and ozone. *Appl. Surf. Sci.* **2022**, *571*, 151231. [CrossRef]

51. Broas, M.; Kanninen, O.; Vuorinen, V.; Tilli, M.; Paulasto-Kröckel, M. Chemically stable atomic-layer-deposited Al$_2$O$_3$ films for processability. *ACS Omega* **2017**, *2*, 3390–3398. [CrossRef]

52. Rahane, A.B.; Deshpande, M.D.; Kumar, V. Structural and electronic properties of (Al$_2$O$_3$)$_n$ clusters with n = 1–10 from first principles calculations. *J. Phys. Chem. C* **2011**, *115*, 18111–18121. [CrossRef]

53. Scandolo, S.; Giannozzi, P.; Cavazzoni, C.; de Gironcoli, S.; Pasquarello, A.; Baroni, S. First-principles codes for computational crystallography in the Quantum-ESPRESSO package. *Z. für Krist. -Cryst. Mater.* **2005**, *220*, 574–579. [CrossRef]

54. Jónsson, H.; Mills, G.; Jacobsen, K.W. Nudged elastic band method for finding minimum energy paths of transitions. In *Classical and Quantum Dynamics in Condensed Phase Simulations*; Berne, B.J.; Ciccotti, G., Coker, D.F., Eds.; World Scientific: Singapore, 1998; pp. 385–404.

55. Jansen, A.P.J. (Ed.) *An Introduction to Kinetic Monte Carlo Simulations of Surface Reactions*; Springer Berlin: Heidelberg, Germany, 2012; Volume 1, pp. 38–119.

56. George, S.M. Atomic Layer Deposition: An Overview. *Chem. Rev.* **2010**, *110*, 111–131. [CrossRef]

57. Schwille, M.C.; Schössler, T.; Schön, F.; Oettel, M.; Bartha, J.W. Temperature dependence of the sticking coefficients of bis-diethyl aminosilane and trimethylaluminum in atomic layer deposition. *J. Vac. Sci. Technol. A* **2017**, *35*, 01B119. [CrossRef]

58. Lee, G.; Lee, B.; Kim, J.; Cho, K. Ozone Adsorption on Graphene: Ab Initio Study and Experimental Validation. *J. Phys. Chem. C* **2009**, *113*, 14225–14229. [CrossRef]

59. Voter, A.F. Introduction to the Kinetic Monte Carlo Method. In Proceedings of the Radiation Effects in Solids, Erice, Sicily, Italy, 17–29 July 2004; pp. 1–23.

60. Li, N.; Marcus, S.D.; Ngo, T.T.; Griffin, K. Gas Separation Control in Spatial Atomic Layer Deposition. Google Patents 11,230,763B2, 25 January 2022.

61. ANSYS. *Ansys Fluent Theory Guide*; ANSYS Inc.: Canonsburg, PA, USA, 2022.

62. Nishiguchi, T.; Saitoh, S.; Kameda, N.; Morikawa, Y.; Kekura, M.; Nonaka, H.; Ichimura, S. Rapid Oxidation of Silicon Using UV-Light Irradiation in Low-Pressure, Highly Concentrated Ozone Gas below 300 °C. *Jpn. J. Appl. Phys.* **2007**, *46*, 2835. [CrossRef]

63. Benson, S.W.; Axworthy, A.E. Mechanism of the Gas Phase, Thermal Decomposition of Ozone. *J. Chem. Phys.* **1957**, *26*, 1718–1726. [CrossRef]

64. Pan, D.; Li, T.; Chien Jen, T.; Yuan, C. Numerical modeling of carrier gas flow in atomic layer deposition vacuum reactor: A comparative study of lattice Boltzmann models. *J. Vac. Sci. Technol. A* **2014**, *32*, 01A110. [CrossRef]

65. Shaeri, M.R.; Jen, T.C.; Yuan, C.Y. Reactor scale simulation of an atomic layer deposition process. *Chem. Eng. Res. Des.* **2015**, *94*, 584–593. [CrossRef]

66. Peltonen, P.; Vuorinen, V.; Marin, G.; Karttunen, A.J.; Karppinen, M. Numerical study on the fluid dynamical aspects of atomic layer deposition process. *J. Vac. Sci. Technol. A* **2018**, *36*, 021516. [CrossRef]

67. Elers, K.E.; Blomberg, T.; Peussa, M.; Aitchison, B.; Haukka, S.; Marcus, S. Film uniformity in atomic layer deposition. *Chem. Vap. Depos.* **2006**, *12*, 13–24. [CrossRef]

68. Kim, J.; Chakrabarti, K.; Lee, J.; Oh, K.Y.; Lee, C. Effects of ozone as an oxygen source on the properties of the Al_2O_3 thin films prepared by atomic layer deposition. *Mater. Chem. Phys.* **2003**, *78*, 733–738. [CrossRef]

69. Andreoni, W.; Yip, S. *Handbook of Materials Modeling: Methods: Theory and Modeling*, 2nd ed.; Springer International Publishing: Cham, Switzerland, 2020.

70. Yun, S.; Tom, M.; Ou, F.; Orkoulas, G.; Christofides, P.D. Multiscale Computational Fluid Dynamics Modeling of Thermal Atomic Layer Etching: Application to Chamber Configuration Design. *Comput. Chem. Eng.* **2022**, *161*, 107757. [CrossRef]

71. Lee, J.M.; Lee, J.; Oh, H.; Kim, J.; Shong, B.; Park, T.J.; Kim, W.H. Inhibitor-free area-selective atomic layer deposition of SiO_2 through chemoselective adsorption of an aminodisilane precursor on oxide versus nitride substrates. *Appl. Surf. Sci.* **2022**, *589*, 152939. [CrossRef]

72. Fang, G.; Xu, L.; Ma, J.; Li, A. Theoretical Understanding of the Reaction Mechanism of SiO2 Atomic Layer Deposition. *Chem. Mater.* **2016**, *28*, 1247–1255. [CrossRef]